

1 **Maar-diatreme geometry and deposits: subsurface blast experiments with variable**  
2 **explosion depth**

3

4 Graettinger, A.H.<sup>1</sup>; Valentine, G.A.<sup>1</sup>; Sonder, I.<sup>1</sup>; Ross, P.-S.<sup>2</sup>, White, J.D.L.<sup>3</sup>, Taddeucci, J.<sup>4</sup>

5

6 1 Center for Geohazards Studies, 411 Cook Hall, University at Buffalo, Buffalo, NY, 14260,

7 USA

8 2 Institut national de la recherche scientifique, centre Eau Terre Environnement, 490, Rue de la

9 Couronne, Québec (QC), G1K 9A9, Canada

10 3 Geology Department, University of Otago, Dunedin, New Zealand

11 4 Istituto Nazionale di Geofisica e Vulcanologia (INGV), Roma, Italy

12

This is a preprint version of

Graettinger AH, Valentine GA, Sonder I, Ross P-S, White JDL, Taddeucci J  
(2014) Maar-diatreme geometry and deposits: subsurface blast experiments  
with variable explosion depth. *Geochemistry, Geophysics, Geosystems* 15, DOI  
10.1002/2013GC005198

13 **Abstract**

14 Basaltic maar-diatreme volcanoes, which have craters cut into pre-eruption landscapes  
15 (maars) underlain by downward-tapering bodies of fragmental material commonly cut by  
16 hypabyssal intrusions (diatremes), are produced by multiple subsurface phreatomagmatic  
17 explosions. Although many maar-diatremes have been studied, the link between explosion  
18 dynamics and the resulting deposit architecture is still poorly understood. Scaled experiments  
19 employed multiple buried explosions of known energies and depths within layered aggregates in  
20 order to assess the effects of explosion depth, and the morphology and compaction of the host on  
21 the distribution of host materials in resulting ejecta, the development of sub-crater structures and  
22 deposits, and the relationships between them. Experimental craters were 1-2 m wide. Analysis of  
23 high-speed video shows that explosion jets had heights and shapes that were strongly influenced  
24 by scaled depth (physical depth scaled against explosion energy) and by the presence or absence  
25 of a crater. Jet properties in turn controlled the distribution of ejecta deposits outside the craters,  
26 and we infer that this is also reflected in the diverse range of deposit types at natural maars.  
27 Ejecta were dominated by material that originated above the explosion site, and the shallowest  
28 material was dispersed the farthest. Subcrater deposits illustrate progressive vertical mixing of  
29 host materials through successive explosions. We conclude that the progressive appearance of  
30 deeper-seated material stratigraphically upward in deposits of natural maars probably records the  
31 length and time scale for upward mixing through multiple explosions with ejection by shallow  
32 blasts, rather than progressive deepening of explosion sites in response to drawdown of aquifers.

33 Key points (less than 80 char)

- 34 • Blast experiments successfully recreate maar-diatreme like structures
- 35 • Ejecta distribution is controlled by scaled depth and ground condition

- 36 • Componentry indicates deeply sourced lithics are erupted by multiple blasts
- 37 • Only shallow blasts emplace ejecta to form extra-crater deposits

38

## 39 **1.0 Introduction**

40 Basaltic maar-diatreme volcanoes are the result of multiple subsurface explosions produced by  
41 the interaction of magma and groundwater. This results in a crater below the previous ground  
42 surface, with proximal ejecta forming a low tephra (ejecta) ring, plus distal fall and density  
43 current deposits that cover the surrounding landscape. Beneath the crater a diatreme structure  
44 extends downward in a funnel-like shape and terminates with an irregular root zone (Ross and  
45 White 2011 and references therein). Direct observations of historical maar-diatreme volcanoes  
46 are limited to a few examples, with the best descriptions from the 1977 Ukinrek Maars in Alaska  
47 (Kienle et al. 1980; Self et al. 1980). Detailed descriptions of surface (crater and tephra ring) or  
48 subsurface (diatreme) structures of pre-historic examples of these volcanoes are available from  
49 several locations (e.g., Hearn 1968; White 1991; Brand and Clarke 2009; Valentine et al. 2011;  
50 Ross et al. 2011; White and Ross 2011; Lefebvre et al. 2013), however, there is only one, small  
51 example where the eruptive deposits, landform, and the subsurface diatreme are all preserved  
52 and exposed (Geshi et al 2011). Certainly there are no examples where direct observations of  
53 eruption dynamics can be combined with integrated field data of a maar and its diatreme.

54         Investigations of these volcanoes have helped evolve a model of maar-diatreme  
55 formation, where subsurface explosions occur at multiple depths and lateral locations, and there  
56 is increasing evidence that only shallow explosions produce extra-crater deposits (White and  
57 Ross 2011; Valentine 2012; Valentine and White 2012). Additionally, crater growth is known to  
58 be from a combination of explosive and collapse processes (Hearn 1968; Houser 1969; Ross et

59 al. 2011). Many questions about the relationships between explosion dynamics and the resulting  
60 geological features can only be addressed experimentally; we focus on three sets of questions in  
61 this paper. First, how do explosion energy, depth, and number control maar-diatreme size and  
62 shape? Second, how are lithics that originate at different depths beneath a volcano distributed  
63 onto the surface as a function of explosion energy, depth and number of explosions? Finally,  
64 how do explosion processes control the formation of diatremes, and what is the relationship  
65 between diatreme deposits and erupted deposits? Here we use outdoor, meter-scale, experiments  
66 that simulate subterranean phreatomagmatic explosions in layered media (referred to as pads) to  
67 investigate the deposits and structures produced above and below the surface. The integration of  
68 video observations of depositional processes, “before” and “after” morphological data, and  
69 granulometry and componentry of samples is unique to this experimental setup. The experiments  
70 are essentially small-scale eruptions, but are sufficiently large to scale well with natural  
71 eruptions, and are studied by the same geological and monitoring techniques that would ideally  
72 be used at a real volcano. Unlike natural eruptions, the experiments are conducted with excellent  
73 control on initial and boundary conditions (Valentine et al. 2012; Ross et al., 2013; Taddeucci et  
74 al., 2013).

75         The experiments show that explosion depth, explosion energy, and a combination of pad  
76 conditioning and surface topography all contribute to the size and shape of the resulting jet and  
77 consequently surface expression (crater and distribution of ejecta). Extra-crater deposits (ejecta)  
78 reveal that material escapes the crater with shallow blasts. Consequently, lithics found within  
79 proximal deposits are not directly reflective of the depth of explosion that produced those same  
80 deposits. Multiple subsurface explosions near or below an optimal depth of burial, produce  
81 complex sub-vertical dominal and subsidence structures in the subsurface, resembling

82 diatremes. Deposits that form below the craters (subcrater) are the result of both upward  
83 (explosion-driven) and downward (subsidence) mixing, and produce two major facies.

## 84 **2.0 Methods and definitions**

85 The experiments were conducted using buried chemical explosives (PENTEX booster charges)  
86 of 0.15 to 0.45 kg, with energy density estimated to be  $\sim 5 \times 10^6$  J/kg. The depth of burial and  
87 charge energy were varied in five experiments conducted in compacted, layered aggregate. The  
88 setup is intended to mimic discrete subsurface volcanic explosions in a layered substrate. Natural  
89 phreatomagmatic interactions are known to produce discrete blasts, and studied phreatomagmatic  
90 explosions (molten fuel-coolant interactions, MFCI; Büttner and Zimanowski, 1998) are very  
91 rapid. The detonation wave speed associated with the chemical explosives used in these  
92 experiments is, however, even faster than is expected in an MFCI (Büttner and Zimanowski,  
93 1998) and the initial coupling of explosion energy to the surroundings might differ. Nevertheless,  
94 for the purposes of this investigation, which focuses on large-scale phenomenology and resulting  
95 landforms and deposits, the analogy between chemical and MFCI explosions is reasonable. The  
96 experiments are designed to investigate the relationship between the location of a subsurface  
97 explosion at various energies and the resulting deposits, which can be discussed in terms of  
98 scaled depth:

$$99 \quad D = d/E^{(1/3)},$$

100 where  $d$  = depth of charge burial (depth of material immediately above the charge) and  $E$  is  
101 energy of the explosion in joules with scaled depth units expressed as  $m/J^{1/3}$ .

102

### 103 *2.1 Blast set-up*

104 The blasts were executed in two trenches filled with 15 cm-thick layers, in order from bottom to  
105 top: red gravel (A), pea gravel (B), concrete sand (C), recycled asphalt (D), poorly sorted  
106 limestone sand (E)(Fig. 1; Supplementary Table 1). One trench, which hosted three experiments,  
107 was shallow (75 cm) and contained layers B-E. A second, deeper trench was filled with layers A-  
108 E and hosted two experiments. A 15-30 cm thick layer of mixed aggregate and soil underlay  
109 layer A in both trenches. Each layer was compacted and the final thicknesses were confirmed to  
110 be within +/- 1 cm of the intended 15 cm. The surface of the layered system was covered with a  
111 1 cm-thick layer of white aragonite gravel (coarse sand and granules, Layer F) to serve as a  
112 marker of the flat pre-blast surface. Each experiment was conducted in a 3 m × 3 m ‘pad’ in one  
113 of the trenches where between one and three explosions were executed, for a total of 12 blasts  
114 (Table 1). Each of the five pads also had four ~7.5 cm diameter vertical holes filled with the  
115 white aragonite with a spacing of 25 cm radially away from the explosion epicenters, to serve as  
116 markers of subsurface deformation. The hole for each charge was created using a 10 cm diameter  
117 pipe that was hammered into the pad. The contents of the pipe were removed to enable precise  
118 charge placement with minimal disruption of the artificial strata. The placement of the charge  
119 occurred just before detonation, with a delay of up to one hour between the execution of each  
120 blast. Every charge hole was filled with brown-colored aquarium gravel after the placement of  
121 the charge and pressed by hand, not compacted.

122 Pad 1 had a single 0.45 kg charge buried at its optimal depth for crater excavation (Goto  
123 et al., 2001). Pad 2 had two consecutive and co-located, 0.3 kg charges at the same depth as Pad  
124 1. Pad 3 had three blasts of 0.15 kg each with a different depth of burial that maintained at least  
125 50 cm of immediate overburden. Pads 4 and 5, in the deeper trench, focused on deep blasts (1 m)  
126 with 0.15 kg charges. Pad 4 had a constant charge position, while Pad 5 had a charge position

127 that moved progressively toward the surface. For simplicity, each blast will be referred to by an  
128 abbreviated code of pad number followed by blast number (e.g. PIB1 for Pad 1 Blast 1).

129

## 130 *2.2 Blast observations*

131 The blasts were recorded using a variety of equipment including seismic, acoustic, and electrical  
132 field sensors. Here we focus on high speed (300 fps, 512 x 384 resolution) and high definition  
133 (30 fps, 1920 x 1080 resolution) video that shows the evolution of the blast jets from onset to  
134 deposition. Additional video and geophysical data will be discussed in other publications. The  
135 evolution of jet shapes is described, and important features quantified: maximum jet height,  
136 maximum jet width (top and bottom of jet), the time to the onset of deposition, and the time to  
137 the completion of deposition. The onset of deposition was determined to be the first significant  
138 downward motion of material near the pad surface, and the completion corresponded to the  
139 cessation of motion of coarse material. A dilute dust cloud lingered in the air over the explosion  
140 sites, but did not produce sufficient deposits to sample, so its timing was not calculated.

141 Jet shape is described as a ratio of the width of the top of the jet relative to the base  
142 ( $W_t/W_b$ ), where the base width is the greatest width of the jet at or just above the pad surface,  
143 and top width is defined as the widest diameter of the curve that defines the top of the dense jet  
144 (Fig. 2).  $W_t/W_b$  characterizes the motion of the debris within the jet at its maximum extent  
145 relative to horizontal start position and is independent of height, which was measured separately.  
146 This property is comparable to ‘jet angle’, a measure of the angle between the sides of the jet,  
147 used in Taddeucci et al. (2013).

148

## 149 *2.3 Measurements, excavation and sampling*

150 Following each blast the pad and surrounding area were documented using still photography.  
151 The features produced by each blast include either a broad crater, a pile of material in a  
152 depression (referred to as a retarc; Houser 1969), or a narrow steep-sided subsidence pit. The  
153 final feature of each experimental pad was either a crater or a subsidence pit. Visual observations  
154 were recorded in conjunction with orthogonal topographic profiles of the surface structures  
155 measured at 10 cm intervals. For most blasts a penetrometer (“soil compaction tester” modified  
156 to have a flat circular tip 1 cm in diameter) and/or a metal rod (1.6x 1.0 cm in section,  
157 rectangular shape) was inserted into the subsurface to the point of increased resistance  
158 (compaction profiles); this provides a semi-quantitative measure of the extent of subsurface  
159 disruption of the layered aggregates. Blasts typically decrease the compaction of the aggregate  
160 near the charge position, so when possible (Pad 4 and 5) compaction profiles were collected  
161 between each blast to monitor the progressive changes in compaction resulting from multiple  
162 blasts. The metal rod was used in cases where the length of the penetrometer was insufficient to  
163 reach the depth of compaction. Here we use the term ‘subcrater’ for all structures and deposits  
164 beneath the crater floor; this is not a genetic term implying transport mechanisms.

165 Ejecta is defined here as material thrown from the explosion site and deposited outside  
166 the craters (see also Ross et al., 2013). Ejecta samples were collected in 0.25 m<sup>2</sup> trays arranged in  
167 two radial arrays starting 2 m from each blast epicenter and extending outward to 17 m (Fig. 1).  
168 Box spacing was 1 m (center to center). One additional sample container was placed 1.5 m from  
169 the blast epicenter. Ejecta distribution is described in terms of crater radius as in Lee and  
170 Mazzola (1989) and Gould (1981). Here we divide ejecta into 1) Proximal ejecta, the  
171 topographically high area immediately surrounding the crater rim, where the deposits reach their  
172 maximum thickness; 2) Medial ejecta is a thin but continuous sheet and is here characterized in

173 terms of mass per unit area ( $> 0.1 \text{ kg/m}^2$ ); and 3) Distal ejecta consists of isolated clasts beyond  
174 the medial blanket. The proximal-medial and medial-distal boundaries are somewhat subjective  
175 and in reality are gradational. Componentry of the samples was analyzed to determine the weight  
176 percentage of the different material types in each sample.

177 A ditch was dug along the outer edge of the two experimental trenches after the blasts  
178 were complete. This provided access for cross-sectional examination of the subsurface features  
179 created by the experiments. Each pad was then excavated incrementally with reference photos  
180 and detailed descriptions of vertical faces produced every ca. 20 cm. Samples were collected  
181 from deposits within the crater rim, crater bottom, and subcrater deposits. Subsurface and ejecta  
182 samples were analyzed for componentry. Reference photographs were used to make  
183 measurements of angles and the size of structures in the subsurface to supplement observations  
184 made in the field.

### 185 **3.0 Results: experiments by Pad**

#### 186 **3.1 Pad 1**

187 Pad 1 had one blast at approximately the optimal depth of burial for maximum crater excavation,  
188 defined by a scaled depth of  $0.0035 \text{ m/J}^{1/3}$  (Table 1; Goto et al. 2001). At this scale 0.45 kg was  
189 buried under 50 cm of aggregate (same as Pad 1 from previous experiments; Valentine et al.  
190 2012). This pad serves as a control to investigate the simple blast system using updated  
191 monitoring processes and complex set up (thinner layers and more instrumentation) and as a link  
192 to the 2012 experiments. It also represents the simplest scenario for comparison with subsequent,  
193 more complicated pad experiments.

194

195 3.1.1 Pad 1 Jet phenomenology, crater morphology and ejecta

196 The blast initially produced a rounded dome that expanded to form discrete fingers having high  
197 particle concentration (Video 1). Deposition began at the base of the jet while expansion  
198 continued at the top, forming an upside-down trapezoid shaped jet (Fig. 2). Most material was  
199 deposited within a few meters of the blast center from direct collapse at the base of the jet, and  
200 then deposition moved progressively outward as jet fingers collapsed. Isolated ejecta clasts  
201 traveled farther and deposition of coarse material took roughly 3 seconds. A dilute cloud of dust  
202 hovered over the site, but did not leave detectable deposits. The single blast at Pad 1 produced a  
203 well-defined crater nearly 2 m in diameter, with an undulating rim and a surrounding subtle  
204 second ring (Fig. 3). Beyond the second rim the deposits were distinctly rayed in map view. Rays  
205 traced back toward the crater rim where they formed distinct ridges extending outward from  
206 highs along the rim. The distribution of rays was irregular, but typically on the order of 10-20 cm  
207 apart at the crater rim.

208 Ejecta deposition (Fig. 4) decreased rapidly with distance ( $4 \text{ kg}\cdot\text{m}^{-2}/\text{m}$ ) out to ~5 m from  
209 the epicenter, followed by a more gradual decrease representing deposition of scattered particles  
210 (distal ejecta). This trend was seen in previous experimental results (Valentine et al. 2012).  
211 Ejecta travelled up to 16 m from the blast center and was composed of materials from the top  
212 four pad layers (overwhelmingly layers D and E, i.e. the top 30 cm of the pre-blast stratigraphy,  
213 plus the ground marker layer F), plus aquarium gravel from the charge hole (Fig. 5). The greatest  
214 depth of excavation as inferred from ejecta componentry was 0.45 m, just 5 cm above the  
215 emplaced charge (0.5 m below the pad surface). Ejecta were enriched in layer D clasts near the  
216 crater, but D clasts were progressively replaced by layer E and layer F clasts (derived from  
217 shallower depths in the pad) with increasing distance. Up to 5% of layer B material (in which the

218 charge was placed) was detected in the proximal ejecta. Minor amounts (ca. 1.5 wt. %) of layer  
219 B were collected in the medial ejecta. Black chemical precipitate was common on clasts in the  
220 distal ejecta.

221

### 222 3.1.2 Pad 1 Subsurface structure and deposits

223 Excavation of Pad 1 revealed deposits in the immediate subcrater that displayed weakly  
224 developed bedding following the curved inner wall of the crater (Fig. 6 and 7). The components  
225 of the deposits were mixed, with local centimeter to decimeter scale domains dominated by  
226 individual material types. We use the term ‘domain’ to describe a body having relatively  
227 consistent internal composition within a deposit, but which is not a bed or layer. These layered  
228 deposits had sharp basal contacts. Below the bedded subcrater deposits were deposits comprising  
229 vertically concentric domains in which unmixed deeper layer C occurred at the center of the  
230 structure. The margins of the domainal subcrater structure were defined by a lateral transition  
231 from preexisting layers into deformed, inward dipping layers that extended into steeply angled  
232 domains within the concentric structure. Material from layer B was not present in the vertical  
233 domains, but instead had a synformal structure below the crater. The compaction profile reached  
234 a depth of 0.80 m below the original pad level (Table 2). Laterally the profile (slope of 68°)  
235 corresponded with the transition from undeformed host layers to downward-deformed layers.  
236 Beyond the crater rim, the original layers show an apparent outward dip. This phenomenon was  
237 also reported by Ross et al. (2013) for a comparable experiment.

238         In the following we continue to describe subcrater deposits as either bedded or domainal.  
239 Bedded deposits contain layers that are parallel or subparallel to the bounding surfaces of the  
240 facies (the base of the bedded deposits approximately parallels the bowl-shaped crater floor).

241 Domainal deposits contain irregularly shaped domains of different compositions that can have  
242 steep to near vertical contacts.

243

## 244 **3.2 Pad 2**

245 Pad 2 had two co-located blasts (Table 1) to investigate the relationship between scaled depth  
246 and a disrupted pad that included a crater, with a focus on the ejection process. The first  
247 explosion occurred near the optimum depth of burial. The second blast occurred in a disturbed  
248 pad under an existing crater, and the immediate overburden was about 27 cm for P2B2, which  
249 was less than the optimal depth of burial ( $2.03 \times 10^{-3} \text{ m/J}^{1/3}$ ). The total explosive energy used in  
250 Pad 2 was 1/3 greater than that used for Pad 1.

251

### 252 3.2.1 Pad 2 Blast 1 Jet phenomenology, crater morphology and ejecta

253 The first blast at Pad 2 produced a broad initial jet with a visible black gas cloud from the  
254 explosive. The ejecta moved upward as a jet comprising numerous individual fingers that was  
255 wider at the top than the base (Fig. 2). Deposition began from the base of the jet, while minor  
256 expansion occurred at the top, so that some (medial) ejecta reached the sample boxes before  
257 upward jet growth ended. A dust cloud lingered above the pad after the main jet collapsed. The  
258 blast produced a 1.5 m diameter, 0.3 m deep crater with a sharp ragged edge, which was  
259 surrounded by a subtle second rim with a height of only a few cm (Fig. 3). The ejecta had a  
260 noticeable rayed distribution, but the associated undulations in the crater rim were subtle. The  
261 rim was prone to collapse.

262 Although the total mass of ejecta collected was less than P1B1, the mass of ejecta per  
263 unit area decayed with increasing distance at a similar rate as for P1B1 (Fig. 4). Distal ejecta

264 travelled up to 15 m from the blast site (Table 1). Ejecta from this blast was dominated by  
265 material from layer E with lesser amounts of clasts from layer F, layer D, and aquarium gravel  
266 (Fig. 5). Material from layer F is dominant further away from the crater, as it was for P1B1. The  
267 greatest depth from which ejecta originated was 0.3 m; the charge was placed at 0.5 m. Debris  
268 from layer D, which forms a good proportion of overall ejecta for P1B1, is nearly absent in the  
269 P2B1 ejecta, although the charges were detonated at the same depth as the previous blast. Black  
270 chemical precipitate was common on clasts in the distal ejecta.

271

### 272 3.2.2 Pad 2 Blast 2 Jet phenomenology, crater morphology and ejecta

273 The jet initiated as a cloud of black gas followed by a mass of debris that rapidly developed into  
274 an expanding jet with individual fingers at its top (Fig. 2). As the jet base expanded the P2B1  
275 crater rim was displaced outward (Video 2). Deposition began at the base, while a dilute dusty  
276 cloud continued to rise. P2B2 increased the crater diameter and produced the deepest crater and  
277 greatest depth to diameter ratio in these experiments (Table 1, Fig. 2). Thinly bedded proximal  
278 ejecta were exposed on the steep inner side of the crater rim, and there were well-defined  
279 slumped masses in the bottom of the crater below. Large clumps of layer E material were  
280 common in the crater bottom with clasts of layer D in a matrix of layer E material.

281 Medial ejecta for this blast only reached 4 m from the blast center, but distal ejecta  
282 traveled as far as 18 m from the blast epicenter, the furthest of any blast within these  
283 experiments. P2B2 ejecta were dominated by layer D clasts, with lesser amounts from layer E  
284 and of aquarium gravel (Fig. 5). The layer D ejecta originated ~0.2 m above the charge position  
285 (Fig. 8). Black chemical precipitate was common on clasts in the distal P2B2 ejecta.

286

287 3.2.3 Pad 2 Subsurface structure and deposits

288 The Pad 2 crater was lined with weakly bedded subcrater deposits of mixed material from layers  
289 C-E (Fig. 6). The crater extended down into layer C, where the bedded subcrater deposits had an  
290 irregular contact with the underlying domainal subcrater deposits. Local domains of layer D  
291 material extended upward, like a folded flap, into the overlying bedded subcrater deposits.  
292 Immediately below the crater, layer C dipped downward and layer B displayed significant  
293 thinning to ~5 cm thickness. The disruption profile extended to a depth of 1.0 m, and profile  
294 edges coincided with the transition between the host material and the deformed, downwarped,  
295 domainal subcrater deposits (Fig. 7). The average profile-edge angle was 50°, significantly less  
296 than for the previous pad.

297

298 **3.3 Pad 3**

299 This pad built on the experience of the 2012 experiments (Valentine et al. 2012), using three  
300 charges in sequence where the scaled depth remained constant, and thus the total depth below the  
301 original pad surface increased. It tested the Lorenz type maar-diatreme model (Lorenz 1986), and  
302 investigated the relationship between explosion depth and the excavation of the host material as  
303 recorded in ballistic deposits (Table 1). All explosions were buried deeper than the optimum  
304 depths for the 0.15 kg charges.

305

306 3.3.1 Pad 3 Blast 1 Jet phenomenology, crater morphology and ejecta

307 The blast initially produced a uniform dome that expanded to form discrete fingers. A distinct  
308 core of aquarium gravel travelled ahead of the rest of the jet (Fig. 8). Deposition began when  
309 lateral expansion of the base stopped. Fines began to loft from the base of the jet as deposition of

310 coarser material continued. As the jet thinned due to deposition, a 26 cm-high retarc became  
311 visible on the pad surface. The retarc appeared to be composed of layer D with a coating of  
312 aquarium gravel within a subtle 1.8 m diameter, 2-3 cm deep circular depression (Fig. 3).  
313 Discrete rays of ejecta (layer E) surrounded the rim of the depression with a spacing of tens of  
314 centimeters.

315         This blast produced minor medial and distal ejecta. The material in the retarc did not  
316 leave the depression and therefore is not considered ejecta. Medial ejecta extended 3 m from the  
317 blast site with the same geometric spreading ( $1/r^2$  decay) dominated distribution as observed in  
318 P1B1 and P2B1 (Fig. 4). Distal ejecta reached only 4 m from the blast site. The ejecta contained  
319 material from the surface layers E and F and trace amounts of layer D ( $< 1$  wt. %; Fig. 9). The  
320 charge originated 0.5 m below the pad but ejected material mostly from depths less than 0.15 m.

321

### 322 3.3.2 Pad 3 Blast 2 Jet phenomenology, crater morphology and ejecta

323 The blast produced initial deformation of the P3B1 retarc from its base, and then the whole mass  
324 rose as material jetted from the slopes of the retarc. The jet shape was dominated by outward  
325 expansion (Fig. 8; Video 3). After the deposition of coarser clasts, a ground-hugging cloud of  
326 fines lingered at the site before dissipating. P3B2 produced a more typical crater, but with a  
327 smaller diameter than that of the depression caused by the first blast (Fig. 3). The crater had a  
328 subtly undulating rim. The inside surface of the crater was dominated by larger clasts from layer  
329 D.

330         Blast 2 produced proximal (up to 14 cm thick) and minor medial ejecta. The mass of  
331 material collected from the second blast was less than the first, but medial ejecta extended to 4 m  
332 beyond the blast epicenter. Distal ejecta was minor, but was collected up to 5 m from the blast

333 site. Ejecta from Blast 2 was dominated by material from layer D with < 10 wt. % of material  
334 from layers E and F (Fig. 9). The blast occurred at 0.4 m below the original pad surface, and  
335 material was ejected from < 0.3 m (base of layer D).

336

### 337 3.3.3 Pad 3 Blast 3 Jet phenomenology, crater morphology and ejecta

338 The whole pad area deformed before a jet rose from the center of the previous crater. As  
339 deposition began at the base of the crater, dusty gas escaped laterally as it was expelled from the  
340 collapsing, coarser-grained mixture that collapsed back into the crater (Fig. 8). The final crater  
341 was slightly larger in diameter, but smaller depth to diameter ratio, than the previous blast (Table  
342 1; Fig. 3). The crater walls had steep 1-3 cm high edges along the rim.

343 This blast produced limited ejecta so that rays of deposits from P3B1 blast were still  
344 discernible on the pad surface. Medial ejecta extended only 2 m from the center, with distal  
345 ejecta reaching 4 m from the blast center. The componentry of these ejecta was diverse, with a  
346 preponderance of layer D clasts and aquarium gravel (Fig. 9). The remaining ejecta comprised  
347 small amounts of layer C, layer E and layer F clasts. While this charge was placed at 0.74 m,  
348 material was ejected only from a depth of < 0.45 m (base of layer C). Proximal ejecta for P3B3  
349 consisted predominantly of mixed layer E and layer F clasts.

350

### 351 3.3.4 Pad 3 Subsurface structure and deposits

352 The subsurface structure produced by the three blasts included well-developed bedded subcrater  
353 deposits to a depth of 0.4 m below the original pad surface and domainal subcrater deposits to a  
354 depth of 0.75 m (Fig. 6). The compaction profile showed disruption 1 m below the pad surface,  
355 which was 0.26 m below the deepest charge in the experiment. The bedded subcrater deposits

356 included discontinuous, centimeter-thick lenticular beds parallel to the crater floor and contained  
357 clasts from all of the layers forming this pad (B-E) except for the surface layer F, which was  
358 completely removed from the crater area. Interbedded with the mixed materials were beds of  
359 unmixed materials from layers B-E. The domainal subcrater deposits included vertically  
360 concentric domains of material from layers B, C and D. Layer E was disrupted within the  
361 diameter the crater, but was not as greatly deformed as the lower units (Fig. 6). The contacts  
362 between units in the subcrater deposits were irregular, with complicated folds along near-vertical  
363 boundaries. Outside of the disrupted zone, layer C contained downward propagating tension  
364 cracks filled with material from overlying layer D. The disruption profile was broad near the  
365 surface and steep at the center, with an average slope of 39°.

366

### 367 **3.4 Pad 4**

368 Pad 4 and 5 focused on deeply buried charges. All charges in Pad 4 were detonated at the same  
369 depth of 1 m below the original pad surface to investigate the potential for mixing in the  
370 subsurface with repeated, co-located explosions such as might occur at a stationary water table or  
371 other fixed volcanic explosion site in a natural maar-diatreme (Table 1).

372

#### 373 3.4.1 Pad 4 Blast 1 Jet phenomenology, crater morphology and ejecta

374 This blast produced upward doming of the whole pad surface followed by the growth of a very  
375 small (~30 cm high) jet (Fig. 8). The jet fell back to the pad surface without significant alteration  
376 to the surrounding pad. No gas venting or fines escape was observed (Video 4). A small central  
377 area subsided after deposition had ceased to form a small pit (we use the term 'pit' to distinguish  
378 depressions formed dominantly by subsidence from craters, formed mainly by explosive

379 excavation). No ejecta escaped the central pit. A series of subtle, concentric surface undulations  
380 could be seen in the distribution of aragonite on the pad surface (Fig. 3).

381

#### 382 3.4.2 Pad 4 Blast 2 Jet phenomenology, crater morphology and ejecta

383 This blast produced a short central jet shaped like a stretched dome (Fig. 8). The jet collapsed  
384 back into the pit, expelling a fine-grained density current that flowed radially outward. Ring  
385 fractures formed around the crater as deposition was complete. All material was deposited in the  
386 pit (no ejecta was collected). A shallow (12 cm deep from the rim) circular subsidence pit 80 cm  
387 across was formed, nearly twice the diameter of the previous pit, ringed by open concentric  
388 fractures (Fig. 3). The circular pit was located within a gently domed area ca. 5 cm high relative  
389 to the original surface of the pad. The pit floor was noticeably disrupted, unlike in the first blast,  
390 revealing material from layer E.

391

#### 392 3.4.3 Pad 4 Blast 3 Jet phenomenology, crater morphology and ejecta

393 This third blast caused the ground surface to rise and initially closed the fractures produced by  
394 the previous blast. A small dome-shaped jet formed with a diameter constrained by the crater  
395 (Fig. 8). A cloud of fines hovered over the jet, and then both the coarse and fine material  
396 collapsed back into the pit (no ejecta was collected). P4B3 produced a pit slightly larger than  
397 Blast 2 (Table 1), but the margins were subtle and domed, rather than fractured (Fig. 3). The  
398 floor of the pit was more homogenous in color as the two surface units (E, F) were mixed.

399

#### 400 3.4.4 Pad 4 Subsurface structure and deposits

401 Excavation revealed a deep subcrater structure that consisted of centrally downwarped pad  
402 layers. No bedded subcrater deposits were observed, but there was minor disruption and mixing  
403 of material from layer F and E in the upper centimeter of the crater floor. The downwarped  
404 layers had variable thicknesses, but vertically bounded domains were absent (Fig. 6 and 7). At  
405 the center of the structure layer B increased in thickness by 10 cm. Layer A was approximately  
406 20 cm thick at the center of the structure, but thinned dramatically to a few centimeters towards  
407 the side of the structure. The disrupted zone, determined by penetrometer, corresponded with the  
408 final depth of layer A, which was 20 cm below the depth of charge placement. Disruption  
409 profiles were collected after every blast and revealed a widening of the disturbed zone, and  
410 progressive shallowing of the angle of the disruption boundary from 72°, to 63° and finally 51°  
411 by the final blast (Fig. 8, Table 2). Clasts within the central zone of the structure were coated  
412 with a black chemical precipitate (Fig. 6). Samples of the subcrater structure immediately below  
413 the crater and near the depth of charge burial reveal minor mixing of material from layer D into  
414 layer E as well as layer A into layer B.

415

### 416 **3.5 Pad 5**

417 The final pad was used to investigate the influence of upward migrating blasts on mixing in the  
418 subsurface (Table 1). This progressive decrease in the scaled depth (and consequently depth  
419 below pad surface) was hypothesized to produce more complete mixing in the subsurface (Ross  
420 and White 2006; White and Ross 2011).

421

#### 422 3.5.1 Pad 5 Blast 1 Jet phenomenology, crater morphology and ejecta

423 The first blast at Pad 5, with the same conditions as P4B1, produced an upward doming of the  
424 pad with a 0.3 m high jet, centered over the charge position (Fig. 8). The jet collapsed back to the  
425 pad without significant disruption of the surface material. P5B1 produced a minor central  
426 subsidence depression (Fig. 3). The collapse was uneven, with steep-sided fractures on one side,  
427 and slopes on the others. No ejecta were produced by this blast.

428

### 429 3.5.2 Pad 5 Blast 2 Jet phenomenology, crater morphology and ejecta

430 The blast resulted in broad uplift of the pad followed by a wave of fines that escaped from  
431 fractures on the edge of the P5B1 pit. A 0.7 m high, dome-shaped jet was produced within the  
432 limits of the pit and collapsed back into it (Fig. 8) with limited alteration of the pad surface.  
433 P5B2 produced a low angle retarc 8 cm in height within a well-defined subsidence pit (Fig. 3).  
434 The margins of the depression had minor open fractures between the crater and rim. No material  
435 escaped the pit.

436

### 437 3.5.3 Pad 5 Blast 3 Jet phenomenology, crater morphology and ejecta

438 Gas and fines escaped from the retarc before surface deformation began, and then the retarc  
439 expanded outward to form a jet that was constrained by the shape of the P5B2 pit, but expanded  
440 outward, low to the ground (Fig. 8). A low cloud of fines appeared as the coarse ejecta were  
441 deposited, and then dissipated slowly. P5B3 produced a shallow crater with a minor medial  
442 ejecta apron (Fig. 3). The surface of the apron was covered by layer D and a sub-linear deposit of  
443 aquarium gravel. The distal edges of the deposits displayed narrowly spaced, irregular rays. The  
444 inside of the crater had several concentric steps moving downward toward its center. The only  
445 blast of the deep series experiments to produce ejecta, P5B3 ejected the smallest total mass of

446 any blasts. The ejecta contained only materials from the upper 15 cm of the pad (layer E and F  
447 clasts).

448

#### 449 3.5.4 Pad 5 Subsurface structure and deposits

450 Excavation of Pad 5 revealed poorly-developed bedded subcrater deposits and a well-developed  
451 domainal subcrater deposit. The bedded subcrater deposits were thin (5-10 cm), weakly bedded,  
452 and consisted of layer E and D materials with abundant aquarium gravel (5 wt. %). The bedded  
453 subcrater deposits graded laterally into the mixed proximal ejecta of the crater rim. The domainal  
454 subcrater deposits share some similarities to the Pad 4 deposits, but had much greater variability  
455 along unit contacts. The near surface layers D and E had undulatory contacts that dipped  
456 downward at the center of the structure. Layer C had some minor undulations on its upper  
457 contact with layer D, but a more continuous contact with layer B. Notably, while layer C dips  
458 downward, the very center of the structure had local upward injection of layer B into layer C  
459 (Fig. 6). Similarly layer A intrudes into layer B on the scale of a few centimeters. Layer B  
460 displayed significant over-thickening at the center of the structure and extended more than 20 cm  
461 below its original base. Layer A was thinner at center of the structure, but deformed around the  
462 protruding layer B, and extended roughly 15 cm below its original layer boundary. The  
463 disruption profile (Fig. 8) became shallower and broader with each progressive blast, and its  
464 slopes decreased ( $85^{\circ}$ - $50^{\circ}$ ). The base of the final disruption profile was higher in the sequence  
465 than the base of the domainal subcrater deposits (Table 2, Fig. 6). Chemical precipitate was  
466 concentrated at the center of the structure, and extended into the mixed aggregate below layer A  
467 materials. Componentry reveals significant mixing in the lower portion of the domainal subcrater

468 deposits where distinct domains of materials from above and below the main layer are present at  
469 the center of the structure. Beyond the rim of the final crater, most pad layers dip outward.

470

#### 471 **4.0 Integrated interpretation of processes and products**

##### 472 **4.1 Effects of explosion energy, depth, and topography on ejecta distribution**

473 Experiment videos reveal diverse jet shapes for the 12 blasts (Fig. 2 & 8), with significant  
474 similarities to jets of previous subsurface blast experiments (Ohba et al. 2002; Taddeucci et al.  
475 2013). Maximum jet height, duration of deposition, and maximum ejecta distance are, to first  
476 order, inversely related to scaled depth in these experiments and those reported in Valentine et al.  
477 (2012), Ross et al. (2013) and Taddeucci et al. (2013) (Fig. 10; Table 1). Blasts at Pads 4 and 5,  
478 at scaled depths  $> 0.008 \text{ m/J}^{1/3}$ , approximately twice the optimal depth of burial, produced minor  
479 jets ( $< 1.0 \text{ m}$  high) with no ejecta. Ejecta were produced at Pad 5 only when the scaled depth had  
480 decreased to the level of the shallow blast experiments (Table 1). The lack of substantial venting  
481 at Pads 4 and 5 also resulted in considerable deposition of black chemical precipitates from the  
482 explosive in the subsurface.

483 For blasts that produced ejecta, deposit distribution was controlled by jet shape, with  
484  $Wt/Wb > 0.5$  required for deposition of ejecta beyond the crater (Fig. 11 and Table 1), and the  
485 distances reached by medial and distal ejecta are approximately proportional to  $Wt/Wb$  above  
486 this value. This trend is also reflected in the mass per unit area of ejecta (Fig. 4). The two main  
487 factors that affect  $Wt/Wb$  are the scaled depth and the presence or absence of a pre-existing  
488 crater or retarc (see Ohba et al. 2002, and Taddeucci et al. 2013). Both medial and distal ejecta  
489 increase in extent with decreasing scaled depth, until the optimal scaled depth of  $0.004 \text{ m/J}^{1/3}$  is  
490 reached; this corresponds to optimal crater excavation (this study and Bening and Kurtz 1967).

491 For depths shallower than this optimal value, the trends of medial vs. distal ejecta diverge. As  
492 scaled depth decreases, the jet produced has a larger  $W_t/W_b$  and therefore distributes isolated  
493 distal ejecta widely (Ohba et al. 2002). In contrast, the extent of medial ejecta decreases  
494 markedly with jet height as more energy from the blasts is lost to the atmosphere (Fig. 10c).

495 Topography and pre-conditioning (disruption of the pad surface) also influenced jet shape  
496 and deposition patterns. In multiple blast experiments, jets through crater-free surfaces produced  
497 more extensive medial ejecta blankets than did those exiting through disrupted ground with  
498 topography. When jets erupted through a blast crater (e.g., P2B2), the ejecta deposit thinned  
499 more abruptly and the maximum extent of the medial ejecta decreased, because the initial  
500 expansion was vertically focused by the crater and more material simply fell or collapsed back  
501 into the craters instead of forming ejecta (Taddeucci et al. 2013). On the other hand, when the jet  
502 erupted from beneath positive topography (a retarc, i.e. Pad 3), the ejecta thinned less rapidly  
503 away from the crater because the jet had an important low-angle component as it erupted through  
504 the outer (lower) edges of the retarc. There was little high-angle ballistic ejection. For blasts that  
505 originate in disrupted ground, a jet erupted through a crater is vertically focused, while one  
506 erupted through a retarc is laterally focused (Fig. 12).

507 In contrast with medial ejecta distribution, the maximum distance of distal ejecta  
508 (isolated clasts) is not strongly affected by the presence of a crater (Fig. 10c) and instead  
509 correlates only with decreasing scaled depth. This dispersal of individual clasts beyond the more  
510 continuous medial ejecta is characteristic of deposits from discrete blasts, in contrast to those  
511 from continuous eruptions with a sustained plume (Self et al. 1980; Gould et al. 1981; Büchel  
512 and Lorenz 1993). We note that in natural eruptions, which have more fine-grained material in

513 the erupted mixture, even jets that collapse back into the crater might expel a dusty gas that  
514 becomes a pyroclastic density current and move across an ejecta ring (see Valentine et al. 2012).

515         The experimental jets had particle-rich fingers, reflecting varying degrees of gas-particle  
516 coupling. For jets where the width of the top of the jet exceeds that of the width of the base  
517 ( $W_t/W_b > 1$ ), these fingers follow ballistic paths at a range of angles and deposit material in rays  
518 that extend outward from the crater rims. Each finger begins deposition at or near the crater rim  
519 and then sediments progressively outward (Fig. 12), in the same manner that has been  
520 documented for ejecta deposition from impact craters (Melosh 1989). In some cases, fingers of  
521 poorly sorted material produce upon landing small, fine-grained density currents that extend  
522 outward from the finger's depositional axis. These density currents are fed by fine-grained  
523 particles and air that are expelled when coarser material sediments rapidly along the ray axis.  
524 Although we could not sample these fine-grained deposits, the videos record their formation. In  
525 natural volcanic explosions we expect that this process could result in lobate fines-rich deposits  
526 that thin away from a lobe's dispersal axis. They would be similar to lateral-blast deposits with  
527 fines-depleted basal layers and finer grained upper layers and evidence of traction carpet  
528 deposition. Additionally, isolated large clasts often travel at the tips of these jets, or on isolated  
529 paths beyond the distribution of the main body of the jet.

530

#### 531 **4.2 Ejection of shallow- versus deep-seated materials**

532 Medial ejecta deposits were dominated by clasts from strata above the explosion sites (layers F,  
533 E, D, and aquarium gravel). Deposits from the initial blasts at Pads 1-3 were relatively enriched  
534 near the crater in material from layer D, which was progressively replaced by layer E material  
535 and aragonite with increasing distance. In other words, deep-seated materials were not ejected as

536 far as shallow-seated materials. The medial ejecta componentry evolved with each subsequent  
537 blast. Clasts from deeper layers (but still above the explosion site) became enriched in the ejecta  
538 only after multiple blasts (Fig. 9). This is interpreted as due to progressive blast-driven mixing of  
539 materials within subcrater deposits, which form the overburden for subsequent explosions. While  
540 this is accompanied by a depletion of shallow clast types, collapse of the crater rim will return  
541 shallow and recently erupted material to the crater, where it might be re-ejected.

542 Proximal ejecta samples were collected from the crater wall, the high point of the crater  
543 rim, and the deposits just outside the crater rim. While there were limited samples of proximal  
544 ejecta (Pad 1, Pad 3 and Pad 5) the componentry show similarities to medial ejecta for these  
545 blasts. Some proximal samples included deeper materials (layer D, C, and B), but only one blast  
546 in these experiments ejected material excavated from the depth of the charge (Pad 1). This blast  
547 had a scaled depth that was approximately the optimal excavation value of  $\sim 0.004 \text{ m/J}^{1/3}$ . While  
548 pads with multiple blasts excavated progressively deeper material, the ejecta containing material  
549 from the depth of charge placement was notably absent. This suggests that the ejection of deep  
550 lithics results from a complex explosive history with progressive upward mixing in the  
551 subsurface requiring later shallow blasts to enable eruption and deposition of the lithics outside  
552 the crater. Variable blast depth with time and subsequent mixing has been recently inferred from  
553 field data (Valentine 2012; LeFebvre et al., 2013), rather than progressive deepening of  
554 explosion sites (e.g., Lorenz, 1986).

555

#### 556 **4.3 Crater and Subcrater facies and geometry**

557 Each blast produced either a broad crater, a retarc in a shallow depression, or a narrow steep-  
558 sided collapse pit. These record processes dominated by ejection of material from the explosion

559 epicenter, by vertical lofting and fallback of material to the epicenter, or by *in situ* subsidence  
560 around the explosion site respectively. The surface structure, at most explosion epicenters,  
561 evolved in response to multiple explosions in the subsurface and collapses of the crater rim.  
562 Subcrater disruption profiles reveal areas of reduced compaction (i.e., deformation or damage)  
563 immediately beneath the crater and crater rim. The experiments produced disrupted areas that  
564 narrow with depth, and have relatively steep sides that extended below the depth of deepest  
565 charge placement for a given pad (similar to Ross et al., 2013). The average dips of the subcrater  
566 structures' walls, defined by the compaction profiles, ranged from 40 to 85 degrees. For single  
567 blasts, steeper structures resulted from deeper charges. When subsequent blasts produced wider  
568 craters the dips of the subcrater structure walls became progressively less steep. The depth of  
569 damage beneath the charge site increased with decreasing scaled depth. The diameter of the  
570 disruption area always exceeded the diameter of the crater as measured at the surface (Table 2),  
571 but typically corresponded with or was just outboard of evident deformation in the excavated  
572 subcrater deposits.

573         Two major facies were identified in the subcrater deposits: bedded subcrater facies,  
574 which, when present, occur immediately below the crater floor, and domainal subcrater facies  
575 beneath bedded subcrater deposits, if the latter were present. Bedded subcrater deposits were  
576 typically 3-10 cm thick and contained 0.5-3 cm-thick beds of homogeneously mixed aggregate  
577 and beds of unmixed material. The latter can be composed of material that originated just below  
578 the pad surface, or include material from as deep as 0.45 m below the original surface. These  
579 bedded deposits were thickest just beneath the crater bottoms and thinned toward the crater  
580 edges. The thickness of the bedded facies also varied circumferentially within the crater,  
581 corresponding to deposit rays observed at the surface. Bedded subcrater deposits were formed in

582 Pads 1-3, but they were best developed in Pad 3 where the scaled depth is greater than the  
583 optimal scaled depth (Fig. 6).

584 Domainal deposits formed the bulk of the subcrater structures, with domains including:  
585 (1) deformed subsurface material grading laterally into *in situ* pad layers, and (2) displaced  
586 subsurface material with steep to near-vertical boundaries. The margins of domainal subcrater  
587 deposits are distinguished by downward sagging of the pad layers. The gradational transition to  
588 undisturbed pad strata approximately paralleled the disruption profiles as measured by  
589 penetrometers. The central downward synformal sagging of the layers within the subcrater  
590 structures accompanied an increase in thickness of the layers at the centers of the structures,  
591 which commonly extended below the original pad layers into underlying aggregate (5-30 cm; see  
592 especially Pads 4, 5; Fig. 6). The structures resembled a series of stacked bowls with extreme  
593 over-thickening in the lowest units. The contacts between the deformed layers displayed  
594 irregular undulations a few centimeters apart, with amplitudes up to several centimeters (Fig. 6).  
595 Outside the central structures, tension cracks were locally present along the top of one unit, filled  
596 in with material from the overlying unit (3-5 cm deep; Ross et al. 2013). In some cases (Pad 1  
597 and 3) the center of the structure contained concentric vertical domains that protruded upward  
598 from a deeper unit into shallower ones (see esp. Pad 3; Fig. 6).

599 Bedded subcrater deposits extended up to 20 cm below the pad surface, and lay  
600 immediately on top of a concentric domainal subcrater layer containing material from layers B,  
601 C, D and E (Fig. 7). No concentric upward-extending core was formed in the deep-blast  
602 experiment with co-located explosions (Pad 4). In the case of upward moving charges (Pad 5),  
603 however, detailed componentry data and field observations reveal incipient mixing of deep-

604 seated material upward into subcrater deposits that are otherwise dominated by deformed  
605 shallow pad-layer material.

606 Deformation and mixing in the subsurface are related to upward and downward motion of  
607 materials relative to their original positions. Net upward motion was preserved in the vertically  
608 oriented, concentric, dominal deposits, similar to features recorded in diatreme structures under  
609 maar volcanoes (White 1991; Ross et al. 2013, LeFebvre et al. 2013). Upward migration of  
610 material is invoked as an important mixing process (White 1991), typically associated with  
611 debris jets (Ross and White 2006; Ross et al. 2008a, 2008 b; LeFebvre et al., 2013). Net  
612 downward motion was preserved in the synformal experimental structures, which were  
613 associated with the formation of subsidence pits, similar to those formed in contained nuclear  
614 explosion tests (Houser 1969). The steep dips of subcrater deposits implies that explosion-driven  
615 upward motion and syn-eruption subsidence are sufficient to form these dips and do not require  
616 post-eruption compaction to form (Geshi et al. 2011; Delpit et al. in review) although evidence  
617 for post-formational subsidence has been observed at some maar craters (e.g., Brand et al. 2009;  
618 Ross et al. 2011).

619 Upward movement in this system is driven by the disruption of the subsurface by rapid  
620 expansion of gas produced by the chemical explosive. This explosion-driven disruption affects  
621 material in all directions around the charge, including below the charge. The deposits produced  
622 by these experiments and by laboratory experiments (Ross et al. 2008a, 2008b) indicate that the  
623 displacement is dependent on scaled depth. It is only in shallow explosions that some material is  
624 displaced from the subsurface into the atmosphere and ‘erupted.’ Some of the erupted material  
625 may be deposited outside the crater, but much is deposited within the forming crater.

626 In the subsurface, the space produced by the gas expansion and by upward displacement  
627 of material is reoccupied by deposits once upward momentum of overlying material is expended.  
628 This reoccupation is accomplished through lateral and downward motion of layered pad material  
629 (inward slumping) and near-vertical deposition of material carried in an eruptive jet. After the  
630 deposition from the jet (fallback), additional displacement can occur in the form of subsidence of  
631 the material within and below the crater. Video recordings of the deep blasts show that there was  
632 a delay between depositional fallback of jet material and downward sagging of the surface,  
633 which occurred up to 2 seconds after deposition stopped (Pad 4 and 5). The formation of the  
634 subsidence pit without the production of ejecta represents an apparent decrease in volume of the  
635 pad surface, and in excavation the downward disruption of the pad layers appears to have an  
636 anomalous displacement of the mixed aggregate below the constructed layers. Compaction  
637 profiles indicate a decrease in the pad density, which should produce a volume increase (like a  
638 retarc), so these conditions require deformation of the surrounding pad that was not directly  
639 detected by excavation. The potential for explosions to increase the density of material outside  
640 the immediate subcrater structure was revealed by the upward migrating compaction profiles in  
641 Pad 5. Changes in the thickness of aggregate layers near the base and lateral margins of the  
642 subcrater structure are likely important to this change in compaction of the subsurface. These  
643 variations likely are controlled by material properties including sorting and (though not tested  
644 here) saturation. The displacement of the mixed gravel and the dynamic nature of the disrupted  
645 pad density indicate the complexity of the subcrater structure as a product of multiple explosions  
646 and will be considered in future experiments.

647 The experiments indicate that bedded subcrater deposits only form when there is lofting  
648 of material above the pad surfaces; the thickness of bedded deposits increased with repeated

649 blasts and involved recycling of previous fallback material. Significant recycling accompanies  
650 the formation of primary bedded subcrater deposits in natural maar-diatremes (Houghton and  
651 Smith 1993; Lefebvre et al., 2013). In these experiments componentry analyses indicate that  
652 bedded subcrater deposits experienced greater mixing than deeper deposits. This may be  
653 influenced by the small number of blasts used in these experiments. However, and in contrast to  
654 the ejecta (extracrater) deposits, the bedded subcrater deposits from multiple explosions do  
655 include clasts from the depth of explosion. Similar, but less well-developed bedded subcrater  
656 deposits were produced in previous experiments, where only two, thick (30 cm) layers were  
657 present in the pads (Ross et al. 2013). The development of recognizable stratification in the sub-  
658 crater deposits is probably dependent on the range of clast types, number of pad layers, and clast  
659 sizes in the pad strata, as reflected by the differences between these two experimental sets.

660

## 661 **5.0 Application to maar-diatremes**

662 The effect of increasing scaled depth on the transition from crater to retarc to subsidence pit has  
663 been well documented for underground nuclear weapons tests (Benning and Kurtz 1967; Houser  
664 1969; Gould et al. 1981), and were replicated the these experiments. Nuclear tests involved  
665 energies six to nine orders of magnitude larger than our experimental blasts, overlapping and  
666 exceeding the range of energies of realistic volcanic explosions at natural maars (Self et al. 1980;  
667 Taddeucci et al. 2010; Valentine et al. 2011; Valentine and White 2012). An additional potential  
668 scaling issue is the ‘detonation’ wave speeds of volcanic explosions. Phreatomagmatic (molten  
669 fuel-coolant interaction) explosions have been studied experimentally (Büttner and Zimanowski,  
670 1998) with wave speeds that are slower than those of chemical explosives used in our  
671 experiments. Nuclear tests have very different detonation speeds from those of our chemical

672 explosions but the general phenomena are the same. This similarity indicates that different  
673 detonation speeds do not strongly influence crater and ejecta phenomena, consistent with Goto et  
674 al. (2001). The consistency between features of our experiments and those of nuclear tests with  
675 similar scaled depths (see Houser 1969) lends further credence to the arguments of Ross et al  
676 (2013) that our experiments are well scaled for the reproduction of key volcanic explosion  
677 phenomena.

678 Ejecta produced by shallow blast experiments are dominated by material from near-  
679 surface pad layers similar to observations of maar-diatreme volcanoes (Ross et al. 2011;  
680 Valentine 2012; Lefebvre et al. 2013). Deeper-seated material, when present, was deposited near  
681 the crater, with progressively shallower material increasing in abundance with distance from the  
682 crater (cf. Lee and Mazzola 1989; Table 3). Materials from greater depths can be included in  
683 more distal deposits after repeated blasts in the same crater have mixed subcrater deposits and  
684 are ejected by later shallow explosions (Fig. 9). This mixing by repeated blasts in natural maars  
685 would produce both a lateral and vertical trend deposit composition, in which materials from  
686 deeper stratigraphic units are deposited close to the vent early in the eruption, but may be found  
687 in more distal parts of later deposits. Inverse vertical lithic-fragment stratigraphy has been  
688 observed in tephra rings of historical and eroded maar volcanoes (Kienle et al. 1980; Self et al.  
689 1980; White 1991). Proximal deposits can be lost as a maar crater grows, so that portions of this  
690 pattern are missing from the geologic record, because of syn- and post-eruptive collapse of the  
691 crater rim. Furthermore, as a crater develops it acts to focus eruptive jets vertically, so that most  
692 of their material falls back into the crater. This promotes mixing of materials in the shallow part  
693 of a diatreme but reduces the chance of those materials ending up in tephra ring deposits.

694           Because only shallow blasts successfully eject material from the crater, ejecta  
695   componentry reflects a combination of clast recycling and subsurface mixing from repeated  
696   explosions at various depths. A common assumption is that lithics in tephra ring deposits around  
697   maars record explosions at the lithics' depth of origin (e.g., Sheridan and Wohletz 1983; Lorenz  
698   1986; Mattson et al. 2005; Carrasco-Núñez et al. 2007; Sottili et al. 2009, 2012; Jordan et al.  
699   2013; van Otterloo et al. 2013). Only one of the experimental blasts (Pad 1), which was at the  
700   optimal depth of burial for crater excavation and had a flat undisrupted pad surface, ejected  
701   material from the charge depth. While it is true that the presence of a deep-seated lithic can  
702   imply that there was an explosion at its source depth, it is unlikely that the same explosion  
703   ejected the lithic fragment from the crater. Instead, we infer that such lithics are gradually driven  
704   upward in the diatreme, in stages, by the phenomenon of debris jetting (Ross and White 2006;  
705   Ross et al. 2008a, 2008b), until a shallow explosion ejects it. This inference is supported both by  
706   these experiments and by recent studies of maars and diatremes where there are good constraints  
707   on lithic source depths (Valentine 2012; Lefebvre et al 2013). An important implication of these  
708   results is that the appearance of progressively deeper-seated lithics high in the stratigraphy of a  
709   tephra ring does not record deepening of phreatomagmatic explosion sites due to drawdown of  
710   the water table (Lorenz 1986). Rather, the late eruption of more deeply sourced lithics is related  
711   to the time and number of repeated explosions of varying energies and depths needed to drive the  
712   lithic into the upper part of the diatreme with later shallow blasts to eject the lithics out of the  
713   crater (Valentine and White 2012). Further examples of this process of driving lithics upward is  
714   supported by the observation of maars in the Colli Albani Volcanic District (Central Italy),  
715   where a higher degree of rounding and fragmentation experienced by deeper-derived lithics in  
716   comparison to shallower-derived ones reflects a longer period of intra-conduit mixing and

717 milling before ejection (Sottili et al. 2009), and in phreatomagmatic deposits at Easy Chair  
718 volcano in Nevada (USA; Valentine and Cortés, 2013). Similarly, the absence of deep-seated  
719 lithics in a tephra ring does not imply a lack of deep explosions, just that debris from those deep  
720 explosions was not sufficiently driven upward before the eruptive episode ended nor successfully  
721 ejected from the crater by later shallow blasts. Ejecta beds (or bed sets) only record shallow  
722 scaled depth explosions in tephra ring deposits and can be used to estimate minimum numbers of  
723 explosions. Crustal lithics may be used to constrain only minimum depths of explosive activity  
724 within the growing system over its growth history, and not at a specific time.

725         Our experiments reveal a diversity of jet shapes and resulting ejecta deposits, which are  
726 influenced by the position of the explosion and the pad compaction and overlying topography  
727 (flat, crater, or retarc; Figure 12). Natural systems also reveals a diversity of tephra ring deposits  
728 around maar-diatremes: (1) coarse-grained (tuff breccia to lapilli tuff), poorly-sorted massive  
729 deposits that may be related to direct and rapid sedimentation from an eruptive jet; (2) finer-  
730 grained (lapilli tuff to tuff), moderately-sorted, bedded and cross bedded deposits from dilute  
731 pyroclastic density currents; (3) distal ballistics and fine ash fall (Fisher and Waters 1970;  
732 Waters and Fisher 1971; Crowe and Fisher 1973; Schmincke et al. 1973; Self et al. 1980; Sohn  
733 and Chough 1989; Chough and Sohn 1990; Valentine 2012; Jordan et al. 2013; van Otterloo et  
734 al. 2013). Differences between these deposits have previously been interpreted in terms of  
735 distance from the blast source and/or as the result of different explosion mechanisms (e.g.,  
736 phreato-Vulcanian, Ukinrekian; van Oterloo et al., 2013), but experiments reveal that this  
737 diversity could also be related to scaled depth of explosions, the nature of the existing crater (if  
738 present), and the heterogeneous nature of the eruptive jets. For example, the presence of a poorly  
739 sorted, and massive lapilli tuff or tuff breccia in a tephra ring sequence (e.g., Valentine and

740 Cortés, 2013) may be related not to a fundamentally different type of explosion, but to a very  
741 shallow scaled depth and/or absence of a deep crater (Figure 12a), or by jets that are directed  
742 laterally by the presence of a retarc (Figure 12b). Finer-grained dune-bedded tephra ring deposits  
743 may be caused by a vertically focused eruptive jet, because of large scaled depth or confinement  
744 by a crater, where most of the mixture collapses back onto the explosion epicenter but a cloud of  
745 fines and gas (air) is expelled from the collapsing mixture to feed a dilute density current (e.g.,  
746 P3B3 and P5B2 blasts and Valentine et al., 2012; Figure 12c). We infer that collapsing, high-  
747 particle-concentration fingers might produce deposits similar to those from lateral blast deposits  
748 (Belousov et al., 2007) but more localized and not related to a lateral blast *sensu stricto* (Figure  
749 12d).

750 In addition to craters and ejecta, the blasts successfully produced complex subsurface  
751 mixing driven by both subsidence (Hearn 1968) and explosion-driven upward mixing (debris  
752 jets; Ross et al. 2006, 2008; Valentine 2012). The deposits formed by the explosion-driven  
753 mixing were dependent on the scaled depth, with shallow blasts producing bedded subcrater  
754 deposits, and deep blasts contributing to the formation of domainal subcrater deposits. Bedded,  
755 primary subcrater deposits like those here (Pad 1-3) are known from exhumed maar-diatreme  
756 structures like Missouri River Breaks, Montana and Suona Crater, Miyakejima (Geshi et al.  
757 2011; White and Ross 2011; Delpit et al. in review) as well as kimberlite pipes such as Mwadui  
758 kimberlite (Stiefenhofer and Farrow 2004). In our experimental structures the best-developed  
759 vertical domains in the domainal subcrater deposits were produced by fairly shallow blasts near  
760 or just below the optimal scaled depth (Pad 1-3), whereas deeper blasts (Pads 4-5) initiated  
761 subsurface mixing from multiple blasts below the optimal depths of burial.

762 The Suoana maar-diatreme is revealed in natural cross-section in the caldera wall of  
763 Miyakejima volcano (Geshi et al. 2011) and provides an excellent comparison with our  
764 experimental 'maar-diatremes' (Fig 13). Both structures have bedded proximal deposits, bedded  
765 subcrater deposits, and domainal subcrater deposits. Suoana Crater has four proximal tephra  
766 layers, which suggest that a minimum of four shallow explosions formed the maar-diatreme,  
767 potentially similar to the three blasts of the Pad 3 experiment. The boundaries of the subcrater  
768 'diatreme structures' both here and for Suona (Fig. 13) have subsidence along the margin of the  
769 structure. Although Suona displays well-developed fractures, the relative size, deposit types, and  
770 internal structures are highly similar.

## 771 **6.0 Conclusions**

772 The experiments presented here were analogs for subsurface volcanic explosions with different  
773 strengths and positions that produce both subsurface and surface deposits. Appropriate scaling  
774 with natural volcanic explosions is indicated by successful reproduction of structures and  
775 landforms similar to those of maar-diatreme volcanoes (White and Ross 2011). Jet heights and  
776 shapes, and resulting deposition of ejecta, were determined primarily by scaled depth and the  
777 condition of the pad (compacted with no topography or disrupted with a crater or retarc) above  
778 the explosion. Large scaled depths and the presence of a crater both act to vertically focus  
779 eruptive jets and promote collapse back onto the explosion epicenters. Component analyses show  
780 that ejecta deposits are dominated by materials that originated above (rarely at) the explosion  
781 site, and that shallower-seated materials are deposited farther from the craters than are deep-  
782 seated materials. Extracrater deposits are only produced by shallow blasts that eject material  
783 from the near surface that may include crustal lithics that have been moved upward through  
784 subsurface mixing by previous deeper explosions. Subcrater deposits comprise bedded upper

785 parts and domainal lower parts, both of which record mixing of materials from various depths  
786 (mainly above explosion sites). The presence or absence of deep-seated material in ejecta is not  
787 directly related to the depth of a given explosion and those lithics present represent only a  
788 minimum fragmentation/explosion depth. Ejection and deposition processes observed in the  
789 experimental blasts indicate the potential for a range of different tephra ring deposition processes  
790 (fall and flow) simply due to differences in scaled depths of explosions and the pre-explosion  
791 topography.

792         The experiments reported here and in Valentine et al. (2012), Taddeucci et al. (2013), and  
793 Ross et al. (2013), represent a simplified scenario with vertically aligned explosion locations.  
794 Many natural maars show evidence of horizontally migrating or/and multiple coalescing vents  
795 laterally (e.g. Ort and Carrasco-Núñez 2009; Jordan et al. 2013; Nemeth et al. 2012; Son et al.  
796 2012; van Otterloo et a. 2013), which will be the topic of further experimentation. Experiments  
797 to date reveal important trends in the effects of subsurface explosions, where the most significant  
798 hazards show a trend of ‘peak’ behavior with optimal scaled depth: ejecta distance, duration of  
799 jet (deposition time), and crater size. Such integrated experimental deposits are necessary to  
800 improve our models of natural phenomena.

801

## 802 **7.0 Acknowledgments**

803 These experiments were funded primarily by the University at Buffalo through the UB Center for  
804 Geohazards Studies, with additional contributions from team member sponsors (including  
805 NSERC: Discovery grant to P.-S.R), and were conducted at the Geohazards Field Station. M.  
806 Manoranjan, B. Zimanowski, A. Schmid, D. Gaudin, D. Bowman, K. Keehoon, U. Kueppers,  
807 and G. Lube are thanked for their participation in this project. We also thank the following for

808 their key assistance in preparing for and executing the experiments: D. Goralski, J.L. Ball, K.  
809 Bennet, D. Doronzo A.G. Harp, C.G. Hughes, P. Johnson, S. Pansino, D. Ruth, D. Schonwalder,  
810 M. Sweeney, and P. Moretti. The manuscript was improved through helpful reviews by B. Brand  
811 and Y.K. Sohn.

812

## 813 **7.0 References**

814 Belousov, A. (2006), Distribution and eruptive mechanism of maars in the Kamchatka Peninsula,  
815 *Doklady Earth Sciences*, 406, 24-27. doi:10.1134/S1028334X06010077.

816 Bening, R. G., and M. K. Kurtz (1967), The formation of a crater as observed in a series of  
817 laboratory- scale cratering experiments *Rep.*, p. 63 pp, U.S. Army Engineer Nuclear Cratering  
818 Group, Livermore CA.

819 Brand, B. D., and A. B. Clarke (2009), The architecture, eruptive history, and evolution of the  
820 Table Rock Complex, Oregon: From a Surtseyan to an energetic maar eruption, *Journal of*  
821 *Volcanology and Geothermal Research*, 180, 203-224. doi: 10.1016/j.jvolgeores.2008.10.011.

822 Brand, B.; Clarke, A.; Semken, S. (2009), Eruptive conditions and depositional processes of  
823 Narbona Pass Maar volcano, Navajo volcanic field, Navajo Nation, New Mexico (USA), *Bulletin*  
824 *of Volcanology*, 71, 49-77. DOI: 10.1007.s00445-008-0209-y.

825 Büchel, G., and V. Lorenz (1993), Syn- and post-eruptive mechanism of the Alaskan Ukinrek  
826 Maars in 1977, *Lecture Notes in Earth Sciences*, 49, 15-60.

827 Büttner, R., and B. Zimanowski (1998), Physics of thermohydraulic explosions, *Physical Review*  
828 *57*, 5726-5730.

829 Carrasco-Núñez, G., M. H. Ort, and C. Romero (2007), Evolution and hydrological conditions of  
830 a maar volcano (Atexcac crater, Eastern Mexico), *Journal of Volcanology and Geothermal*  
831 *Research*, 159, 179-197. doi: 10.1016/j.jvolgeores.2006.07.001.

832 Chough, S. K., and Y. K. Sohn (1990), Depositinal mechanics and sequences of base surges,  
833 Songaksan tuff ring, Cheju Island, Korea, *Sedimentology*, 37, 1115-1135.

834 Delpit, S., P.-S. Ross, and B. C. Hearn (in review), Deep bedded ultramafic diatremes in  
835 Missouri River Breaks volcanic field, Montana, USA: more than 1 km of syn-eruptive  
836 subsidence, *Bulletin of Volcanology*.

837 Fisher, R. V., and A. C. Waters (1970), Base surge bed forms in maar volcanoes, *American*  
838 *Journal of Science*, 268, 157-180.

839 Geshi, N., K. Németh, and T. Oikawa (2011), Growth of phreatomagmatic explosion craters: A  
840 model inferred from Suoana crater in Miyakejima Volcano, Japan, *Journal of Volcanology and*  
841 *Geothermal Research*, 201, 30-38. doi: 10.1016/j.jvolgeores.2010.11.012.

842 Goto, A., and H. Taniguchi (2001), Effects of explosion energy and depth to the formation of  
843 blast wave and crater: Field explosion experiment for the understanding of volcanic explosion,  
844 *Geophysical Research Letters*, 28, 4287-4290.

845 Gould, K., and K. Tempo (1981), High-explosive Field Tests: Explosion phenomena and  
846 environmental impacts *Rep.*, Defense nuclear agency Santa Barbara, California.

847 Hearn, C. B. (1968), Diamteres with Kimberlitic affinities in North-Central Montana *Science*,  
848 159(3815), 622-625.

849 Houghton, B. F., and R. T. Smith (1993), Recycling of magmatic clasts during explosive  
850 eruptions: estimating the true juvenile content of phreatomagmatic volcanic deposits, *Bulletin of*  
851 *Volcanology*, 55, 414-420.

852 Houser, F. N. (1969), Subsidence related to underground nuclear explosions, Nevada Test Site,  
853 *Bulletin of the Seismological Society of America*, 59(6), 2231-2251.

854 Jordan, S. C., R. A. F. Cas, and P. C. Hayman (2013), The origin of a large (>3 km) maar  
855 volcano by coalescence of multiple shallow craters: Lake Purrumbete maar, southeastern  
856 Australia *Journal of Volcanology and Geothermal Research*, 254, 5-22. doi:  
857 10.1016/j.jvolgeores.2010.11.012.

858 Kienle, J., P. R. Kyle, S. Self, R. J. Motyka, and V. Lorenz (1980), Ukinrek Maars, Alaska, I.  
859 April 1977 eruption sequence, petrology and tectonic setting, *Journal of Volcanology and*  
860 *Geothermal Research*, 7, 11-37.

861 Kwon, C. W., and Y. K. Sohn (2008), Tephra-filled volcanoclastic neck (diatreme) of a mafic tuff  
862 ring at Maegok, Miocene Eoil Basin, SE Korea, *Geosciences Journal*, 12(4), 1-13. doi:  
863 10.1007/s12303-008-0032-7.

864 Lee, C. K. B., and T. A. Mazzola (1989), Ejecta scaling laws for craters in dry alluvial sites,  
865 *Journal of Geophysical Research*, 94, 17595-17605.

866 Lefebvre, N. S., J. D. L. White, and B. A. Kjarsgaard (2013), Unbedded diatreme deposits reveal  
867 maar-diatreme forming eruptive processes: Standing Rocks West, Hopi Buttes, Navajo Nation,  
868 USA, *Bulletin of Volcanology*, 75, 739. doi: 10.1007/s00445-013-0739-9.

869 Lorenz, V. (1986), On the growth of maars and diatremes and its relevance to the formation of  
870 tuff rings, *Bulletin of Volcanology* 48, 265-274.

871 Lorenz, V., and S. Kurszlaukis (2007), Root zone processes in the phreatomagmatic pipe  
872 emplacement model and consequences for the evolution of maar-diatreme volcanoes, *Journal of*  
873 *Volcanology and Geothermal Research*, 159, 4-32. doi: 10.1016/j.jvolgeores.2006.06.019.

874 Lutz, H., V. Lorenz, T. Engel, F. Häfner, and J. Haneke (2013), Paleogene phreatomagmatic  
875 volcanism on the western main fault of the northern Upper Rhine Graben (Kisselwörth diatreme  
876 and Nierstein-Astheim Volcanic System, Germany), *Bulletin of Volcanology*, 75, 741-755. doi:  
877 10.1007/s00445-013-0741-2.

878 Melosh, H. J. (1989), *Impact Cratering. A Geologic Process*, Clarendon Press. , Oxford.

879 Ohba, T., H. Taniguchi, H. Oshima, M. Yoshida, and A. Goto (2002), Effect of explosion energy  
880 and depth on the nature of explosion cloud. A field experimental study *Journal of Volcanology*  
881 *and Geothermal Research*, 115, 33-42.

882 Ort, M. H., and G. Carrasco-Núñez (2009), Lateral vent migration during phreatomagmatic and  
883 magmatic eruptions at Tecuítlapa Maar, east-central Mexico, *Journal of Volcanology and*  
884 *Geothermal Research*, 181, 67-77. doi: 10.1016/j.jvolgeores.2009.01.003.

885 Ross, P. S., and J. D. L. White (2006), Debris jets in continental phreatomagmatic volcanoes: A  
886 field study of their subterranean deposits in the Coombs Hills vent complex, Antarctica *Journal*  
887 *of Volcanology and Geothermal Research*, 149, 62-84. doi: 10.1016/j.jvolgeores.2005.06.007.

888 Ross, P. S., J. D. L. White, B. Zimanowski, and R. Büttner (2008)a, Multiphase flow above  
889 explosion sites in debris-filled volcanic vents: Insights from analogue experiments, *Journal of*  
890 *Volcanology and Geothermal Research*, 178, 104-112. doi: 10.1016/j.jvolgeores.2008.01.013.

891 Ross, P.-S., J. D. L. White, B. Zimanowski, and R. Büttner (2008)b, Rapid injection of particles  
892 and gas into non-fluidized granular material, and some volcanological implications *Bulletin of*  
893 *Volcanology*, 70, 1151-1168. doi: 10.1007/s00445-008-0230-1.

894 Ross, P.-S., S. Delpit, M. J. Haller, K. Németh, and H. Corbella (2011), Influence of the  
895 substrate on maar-diatreme volcanoes- An example of a mixed setting from the Pali Aike

896 volcanic field, Argentina, *Journal of Volcanology and Geothermal Research*, 201, 253-271. doi:  
897 10.1016/j.jvolgeores.2010.07.018.

898 Ross, P.-S., J. D. L. White, G. A. Valentine, J. Taddeucci, I. Sonder, and R. Andrews (2013),  
899 Experimental birth of a maar-diatreme volcano, *Journal of Volcanology and Geothermal*  
900 *Research*, 260, 1-12. doi: 10.1016/j.jvolgeores.2013.05.005.

901 Schmincke, H.-U., R. V. Fisher, and A. C. Waters (1973), Antidune and chute and pool  
902 structures in the base surge deposits of the Laacher See area, Germany, *Sedimentology*, 20, 553-  
903 574.

904 Self, S., J. Kienle, and J.-P. Huot (1980), Ukinrek Maars, Alaska, II. Deposits and formations of  
905 the 1977 craters, *Journal of Volcanology and Geothermal Research*, 7, 39-65.

906 Sohn, Y. K., and S. K. Chough (1989), Depositional processes of the Suwolbon tuff ring, Cheju  
907 Island (Korea), *Sedimentology*, 36, 837-856.

908 Son, M., J. S. Kim, S. Jung, J. S. Ki, M.-C. Kim, and Y. K. Sohn (2012), Tectonically controlled  
909 vent migration during maar-diatreme formation: An example from a Miocene half-graben basin  
910 in SE Korea, *Journal of Volcanology and Geothermal Research*, 223-224, 29-46. doi:  
911 10.1016/j.jvolgeores.2012.02.002.

912 Sottili, G., J. Taddeucci, D. M. Palladino, M. Gaeta, P. Scarlato, and G. Ventura (2009), Sub-  
913 surface dynamics and eruptive styles of maars in the Colli Albani Volcanic District, Central  
914 Italy, *Journal of Volcanology and Geothermal Research*, 180, 189-202. doi:  
915 10.1016/j.jvolgeores.2008.07.022.

916 Sottili, G., D. M. Palladino, M. Gaeta, and M. Masotta (2012), Origins and energetics of maar  
917 volcanoes: examples from the ultrapotassic Sabatini Volcanic District (Roman Province, Central  
918 Italy), *Bulletin of Volcanology*, 74, 163-186. doi: 10.1007/s00445-011-0506-8.

919 Stiefenhofer, J., and D. J. Farrow (2004), Geology of the Mwadui kimberlite, Shinyanga district,  
920 Tanzania *Lithos*, 76, 139-160. doi: 10.1016/j.lithos.2004.04.017.

921 Taddeucci, J., G. A. Valentine, I. Sonder, J. D. L. White, P.-S. Ross, and P. Scarlato (2013), The  
922 effect of pre-existing crater on the initial development of explosive volcanic eruptions: An  
923 experimental investigation, *Geophysical Research Letters*, 40, 507-510. doi:10.1002/grl.50176.

924 Valentine, G. A. (2012), Shallow plumbing systems for small-volume basaltic volcanoes, 2:  
925 Evidence from crustal xenoliths at scoria cones and maars, *Journal of Volcanology and*  
926 *Geothermal Research*, 223-224, 47-63. Corrigendum 239-240, 111-114. doi:  
927 10.1016/j.jvolgeores.2012.01.012.

928 Valentine, G.A., and J.A. Cortés (2013) Time and space variations in magmatic and  
929 phreatomagmatic eruptive processes at Easy Chair (Lunar Crater Volcanic Field, Nevada, USA),  
930 *Bulletin of Volcanology*, 75, 752. doi: 10.1007/s00445-013-0752-z.

931 Valentine, G. A., and J. D. L. White (2012), Revised conceptual model for maar-diatremes:  
932 Subsurface processes, energetics, and eruptive products, *Geology*, 40(12), 1111-1114. doi:  
933 10.1130/G33411.1.

934 Valentine, G.A., Shufelt, N.L., and A.R.L. Hintz (2011) Models of maar volcanoes, Lunar Crater  
935 (Nevada, USA), *Bulletin of Volcanology*, 73, 753-765. doi: 10.1007/s00445-011-0451-6.

936 Valentine, G. A., J. D. L. White, P.-S. Ross, J. Amin, J. Taddeucci, I. Sonder, and P. J. Johnson  
937 (2012), Experimental craters formed by single and multiple buried explosions and implications  
938 for volcanic craters with emphasis on maars, *Geophysical Research Letters*, 39, L20301.  
939 doi:10.1029/2012GL053716.

940 Waters, A. C., and R. V. Fisher (1971), Base surges and their deposits: Capelinhos and Taal  
941 Volcanoes, *Journal of Geophysical Research*, 76(23), 5596-5614.

- 942 White, J. D. L. (1991), Maar-diatreme phreatomagmatism at Hopi Buttes, Navajo Nation  
943 (Arizona), USA, *Bulletin of Volcanology*, 53, 239-258.
- 944 White, J. D. L., and P. S. Ross (2011), Maar-diatreme volcanoes: A review, *Journal of*  
945 *Volcanology and Geothermal Research*, 201, 1-29. doi:10.1016/j.jvolgeores.2011.01.010.
- 946

Table 1: Summary of results about crater morphology, jet shape and duration.													
Pad	Charge number	Charge size (kg)	Scaled depth <sup>a</sup> m/J <sup>1/3</sup>	Depth of charge relative to pad (m)	Crater diameter (average) d (m)	Crater depth (max) h (m) <sup>b</sup>	Height of retarc above pad (max) (m)	h/d	Rim height above pad (average) (m)	Jet shape Wt/Wb <sup>c</sup>	Max jet height (m)	Deposition duration (s)	Greatest distance of ejecta <sup>d</sup>
1	1	0.45	3.8 x10 <sup>-3</sup>	0.5	1.70	0.37	-	0.21	0.06	2.12	14.1	3.0	17
2	1	0.3	4.4 x10 <sup>-3</sup>	0.5	1.53	0.30	-	0.20	0.03	1.47	8.3	2.75	15
	2	0.3	2.0 x10 <sup>-3</sup>	0.5	1.91	0.54	-	0.28	0.09	1.78	8.4	1.93	19
3	1	0.15	5.5 x10 <sup>-3</sup>	0.5	1.80	0.06	0.27	0.03	0.03	0.77	1.7	1.29	2
	2	0.15	5.5 x10 <sup>-3</sup>	0.47	1.37	0.31	-	0.23	0.08	1.37	1.1	0.48	4
	3	0.15	5.5 x10 <sup>-3</sup>	0.74	1.60	0.26	-	0.16	0.08	0.96	3.0	1.96	4
4	1	0.15	1.1 x10 <sup>-2</sup>	1	0.45	0.10 <sup>e</sup>	-	0.21	0.02	0.29	0.3	0.24	-
	2	0.15	9.8 x10 <sup>-3</sup>	1	0.80	0.12 <sup>e</sup>	-	0.15	0.01	0.30	0.3	0.22	-
	3	0.15	9.8 x10 <sup>-3</sup>	1	0.89	0.17 <sup>e</sup>	-	0.19	0.03	0.51	0.3	0.16	-
5	1	0.15	1.1 x10 <sup>-2</sup>	1	0.58	0.09 <sup>e</sup>	-	0.16	0.01	0.20	0.3	0.21	-
	2	0.15	7.9 x10 <sup>-3</sup>	0.8	1.08	0.05 <sup>e</sup>	0.8	0.04	0.02	0.15	0.7	0.55	-
	3	0.15	6.3 x10 <sup>-3</sup>	0.5	1.32	0.37	-	0.28	0.04	1.40	1.9	1.15	3

a= scaled depth is the physical depth of burial divided by the cube root of the energy

b = crater depth from the raised rim

c =  $W_t/W_b$  is the ratio of the width of the top of the jet over the width of the base of the jet

d = expressed as multiples of crater radius

e = subsidence pit

947

Table 2: Measurements pertaining to the subcrater structures.

	Deepest charge (m)	Crater depth (m) <sup>a</sup>	Depth of disruption (m)	Depth of disruption below charge (m)	Diameter of subcrater structure (m) <sup>b</sup>	Ws-Wc/Wc <sup>c</sup>	Slope angle of subcrater structure
P1B1	0.5	0.31	0.81	0.31	2.00	0.22	68
P2B2	0.5	0.45	0.84	0.34	2.05	0.07	51
P3B3	0.75	0.18	1	0.27	2.00	0.29	39
P4B1	1.0	0.08	1.16	0.16	0.90	1.14	72
P4B2	1.0	0.08	0.98	-0.02 <sup>d</sup>	1.60	1.00	63
P4B3	1.0	0.14	1.21	0.21	1.25	0.42	51
P5B1	1.0	0.12	1.28	0.28	0.8	1.0	85
P5B2	0.8	-0.01	1.2	0.4	1.5	0.46	55
P5B3	0.5	0.32	0.88	0.38	1.7	0.31	50

a = a negative value indicates a mound

b= measured along the greatest width of the penetration profile

c =  $Ws-Wc/Wc$  is a ratio reflecting the excess of the subcrater structure relative to the crater diameter.

d= an anomalous value for this penetrometer run may have resulted from the penetrometer striking a stone.

948

949

Table 3: Deposit types compared to natural examples				
Deposit type	Comparison	Location	Reference	Comments
Distal ejecta and medial	Ejecta blankets composed of ash fall, density current deposits and isolate blocks and bombs.	Albano Maar; Rotomahana; Ukinrek; Mt. Gambier; Teshim Maar (Hopi Buttes, USA);  Military blast testing	Giaccio et al. 2007; Lee and Mazzola, 1989; Gould 1981; Benning and Kurtz 1967; Büchel and Lorenz 1993; van Otterloo et al. 2013	Material that is deposited beyond the scope of the collapsing crater and dominated by shallow dips.
Proximal ejecta	Tephra ring	Yangpori (S.Korea); Albano Maar, Fekete-hegy (Hungary); Lunar Crater (USA)	Auer, et al. 2007; White 1991; Lefebvre et al. 2013; Giaccio et al. 2007; Sohn and Chough, 1989; Chough and Sohn, 1990; Valentine et al. 2011	Subject to collapse during crater growth, likely poor preservation of initial deposits.
Bedded subcrater deposits	Bedded diatreme, upper diatreme	Missouri River Breaks (Montana)	Hearn 1968; White and Ross 2011; Delpit et al. in review; Son et al. 2012	Not always present.
Domain-dominated subcrater deposits	Un-bedded diatreme, Lower diatreme	Hopi Buttes; Suoana Crater	Kwon and Sohn 2008; Lefebvre et al. 2012; Lefebvre et al. 2013; White 1991; White and Ross 2011; Ross et al. 2013; Geshi et al. 2011	Product of both subsidence and explosion-driven upward motion.
* Collapse pits are not preserved at Maar volcanoes, but the occurrence of these pits in the experiments represents the subsidence that plays a key role in maar and diatreme development.				

953 **FIGURE CAPTIONS**

954 Figure 1: Schematic of pad set up including sampling bins. Experimental pad set up A) map  
955 view, showing sample boxes, pad spacing and camera positions. B) Cross-section of pits  
956 containing experimental pads to show pre-blast stratigraphy. Pads 1-3 used layers B-F and Pads  
957 4-5 used A-F. Aquarium gravel was used to fill the charge hole after the charge was placed.  
958 Previous experiments (Valentine et al. 2012; Ross et al. 2013; Taddeucci et al. 2013) had a broad  
959 mounded pad surface.

960 Figure 2: Image captures of the peak jet shape from high definition video of blasts from Pad 1  
961 and Pad 2. For each blast jet shape, resulting crater, and probe profiles are included. The  
962 dimensions of the jet width of top/width of bottom (Wt/Wb) are listed on the upper right hand  
963 corner. Charge location is located on the probe profiles. Schematic of a generalized plume with  
964 the parameters used to define the jets (Wt/Wb and height) is included.

965 Figure 3: Post-blast pad surfaces for each blast, as indicated by Pad and Blast number. Black  
966 marks on vertical scales are 10 cm and black scales on the wall in the background are 1 m in  
967 length.

968 Figure 4: Mass per unit area for experimental pads. A) Comparison of ejecta from Pads 1-3  
969 highlighting the change resulting from subsequent blasts. P2B2 interacted with a crater, P3B2  
970 interacted with a retarc. The videos revealed that due to billowing of the sample bags for P1B1  
971 some volume of ballistic samples were not collected in the first sample bins for P1B1. This  
972 means that mass values for these first bin is considered a minimum value. B) Pads 1-3  
973 overlapping with a logarithmic scale to highlight the increased variation that occurs in the distal  
974 eject noted with dashed line ( $<0.1 \text{ kg/m}^2$ ). C) Comparison of initial blasts through undisturbed  
975 pads from 2013 to 2012 (Valentine et al. 2012).

976 Figure 5: Concentration (mass per unit area) of medial and distal ejecta for Pads 1 and 2.  
977 Componentry at several positions from the blast center are presented in histograms of weight  
978 percent concentration. Stratigraphic layers are B-F in order from bottom to top, and aquarium  
979 gravel was used to fill the charge hole.

980 Figure 6 Excavation cross-sections of blast sites for all pads. Colors represent different  
981 components that are consistent throughout the figures. Sample locations and blast positions are  
982 noted along with final penetrometer profiles. Detailed images and schematics are provided for  
983 proximal ejecta, bedded subcrater deposits and a map view of domainal subcrater deposits are  
984 included. Fine detail of surface morphology was not preserved between the formation of the  
985 craters and excavation due to protective tarps and precipitation.

986 Fig. 7: Simple map showing the spatial distribution of materials in subcrater deposits as they  
987 would be exposed with the removal of subcrater deposits and ejecta. This highlights the  
988 concentric nature of the deformation and dominance of shallow units in these structures.

989 Figure 8: Image captures from high definition video of Pads 3-5. For each blast jet shape,  
990 resulting crater, and probe profiles are included. The dimensions of the jet width of top/width of  
991 bottom (Wt/Wb) are listed on the upper right hand corner. Charge location is located on the  
992 probe profiles. Scales have 10 cm vertical increments. The legend is found on Figure 2.

993 Figure 9 Componentry of medial ejecta from Pad 2 and Pad 3 reflecting the evolution of the  
994 ejecta with each subsequent blast.

995 Figure 10 Jet properties compared with scaled depth A) jet height, B) duration of deposition and  
996 C) distance of distal and medial ejecta. Distal ejecta distribution and duration of deposition both  
997 peak at the optimal scaled depth (highlighted by the black line). The distance of distal ejecta  
998 collection, however, continues to increase with decreasing scaled depth (highlighted by the black  
999 line). The shaded area represents the scaled depth range for optimal crater excavation. C)  
1000 Includes data from previous studies (Valentine et al 2012 and unpublished data), and data from  
1001 Bening and Kurtz 1967 single blast cratering experiment are included for comparison.

1002 Figure 11 Relationship between jet shape (width of top of jet over the width of the base) and  
1003 distance of deposition. While there is some scatter, the wider the jet, the greater the distribution  
1004 of ejecta. Jets with a  $Wt/Wb < 0.5$  produce no ejecta.

1005 Figure 12 Cartoon schematics of ejection (left) and deposition (right) processes observed in the  
1006 experiments. Black objects represent relatively coarse clasts. Gray shades represent mixtures of  
1007 particles and gas, with darker shades representing concentrated and relatively poorly sorted  
1008 mixtures, and light shades representing dilute and fine-grained mixtures. Arrows represent  
1009 direction of motion during ejection and deposition. (a) Optimal to shallow scaled depth with flat  
1010 pre-blast topography. (b) Blast beneath a retarc (mound) with ejecta directed laterally around the  
1011 topographic high. (c) Blast with depth greater than optimal scaled depth and/or beneath a pre-  
1012 existing crater. (d) Detailed side and top views of depositional phase of a clast-rich finger from  
1013 an erupted jet.

1014 Figure 13: Comparison of a natural example of a small maar-diatreme in cross-section from  
1015 Miyakejima Japan (image courtesy of Nobuo Geshi) with Pad 3 from these experiments. The  
1016 schematic shows (not to scale) the similar and dissimilar features of the two sections. Detailed  
1017 descriptions of the Suoana Crater, Miyakejima are available in Geshi et al. 2011. The host rock  
1018 of Suoana crater is alternating pyroclastic deposits and lesser lava.

1019 **Supplementary Material:**

Supplementary table 1: Grain size data for aggregates used in the experiments.

Layer	Mean (mm)	Mode (mm)	Sorting	Maximum grain size (mm)	Skewness	Bulk Density g/cm <sup>3</sup>	Material type
E	1.03	2.8	1.5 poor moderate	4	-0.4	1.3	Crushed limestone
D	11.03	22.6	1.3 moderate	16	-0.6	1.5	Recycled asphalt concrete
C	0.76	0.4	1.4 moderate	4	0.2	1.6	Concrete sand
B	4.59	5.7	0.6 well	16	-0.5	1.4	Limestone pea gravel
A	6.20	5.7	1.2 moderate	8	-0.6	1.4	Red landscaping gravel
AqG	9.11	8.0	0.6 well	8	-0.4	1.4	Aquarium gravel

1020

1021 Video 1:

1022 High definition video of Pad 1 Blast 1 where a 0.45 charge was detonated at a depth of 0.5 cm  
 1023 (optimal scaled depth) in an undisturbed pad with no topography. Black and white scale bars  
 1024 have increments of 10 cm and horizontal black lines on the concrete wall are 1 m long.

1025 Video 2:

1026 High definition video of Pad 2 Blast 2 where the charge was detonated beneath an existing crater  
 1027 in a disrupted pad (0.3 kg charge at 26 cm below the crater bottom, low scaled depth). Black and  
 1028 white scale bars have increments of 10 cm and horizontal black lines on the concrete wall are 1  
 1029 m long.

1030 Video 3:

1031 High speed video (300 frames per second) of Pad 3 Blast 2 where the charge was detonated  
 1032 beneath a retarc (mound) that was produced by a previous blast (0.15 kg charge at 50 cm below  
 1033 the top of the retarc). Black and white scale bars have increments of 10 cm and horizontal black  
 1034 lines on the concrete wall are 1 m long.

1035 Video 4:

1036 High speed video (300 frames per second) of Pad 4 Blast 1 where the charge was detonated in an  
1037 undisturbed pad with no topography, well below the optimal scaled depth (0.15 kg charge at 1  
1038 m). Black and white scale bars have increments of 10 cm and horizontal black lines on the  
1039 concrete wall are 1 m long.

**A**

concrete wall

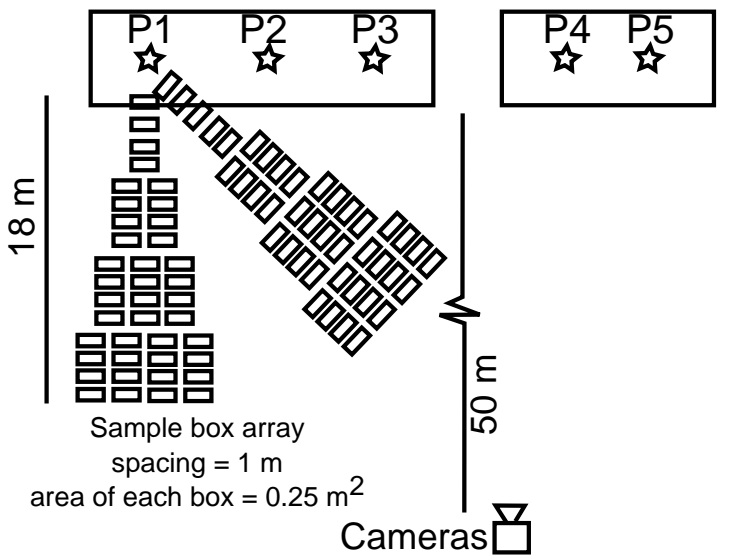
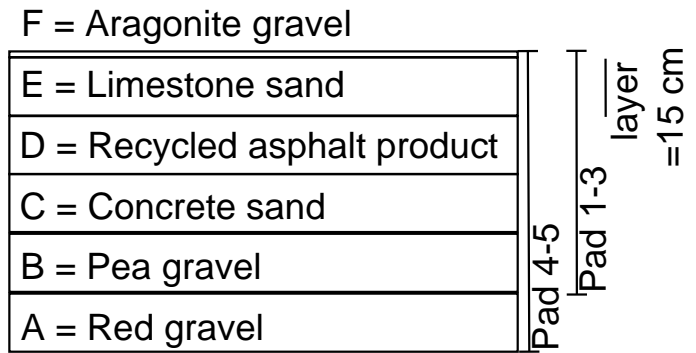
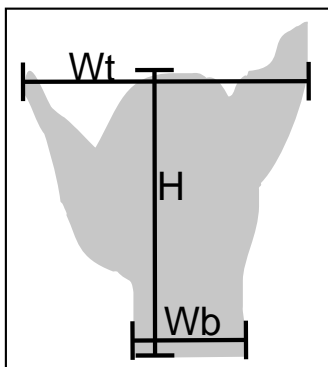
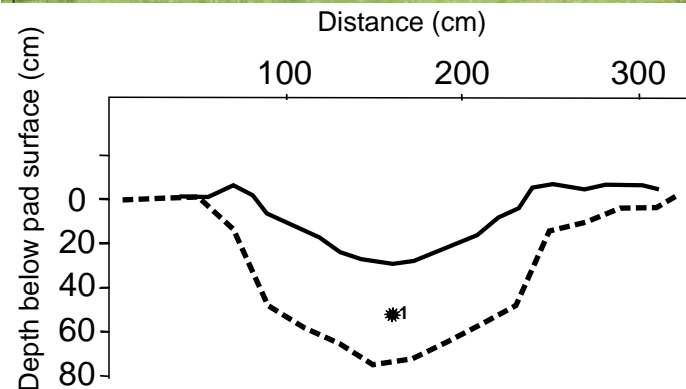
**B**

Figure 1

# Pad1



Wt/Wb 2.12



Pad surface topography

— Blast1

— Blast2

— Blast3

Depth of disrupted zone

- - Blast1

- - Blast2

- - Blast3

★ Charge location

# Pad 2



Wt/Wb 1.47



Blast 2

Wt/Wb 1.78

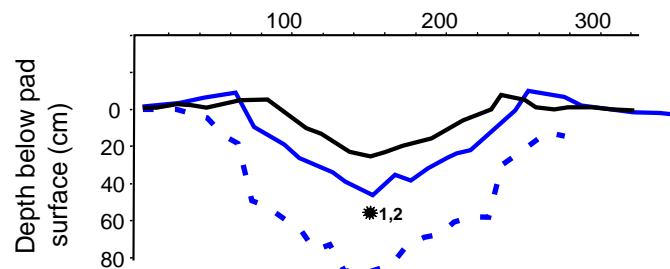


Figure 2

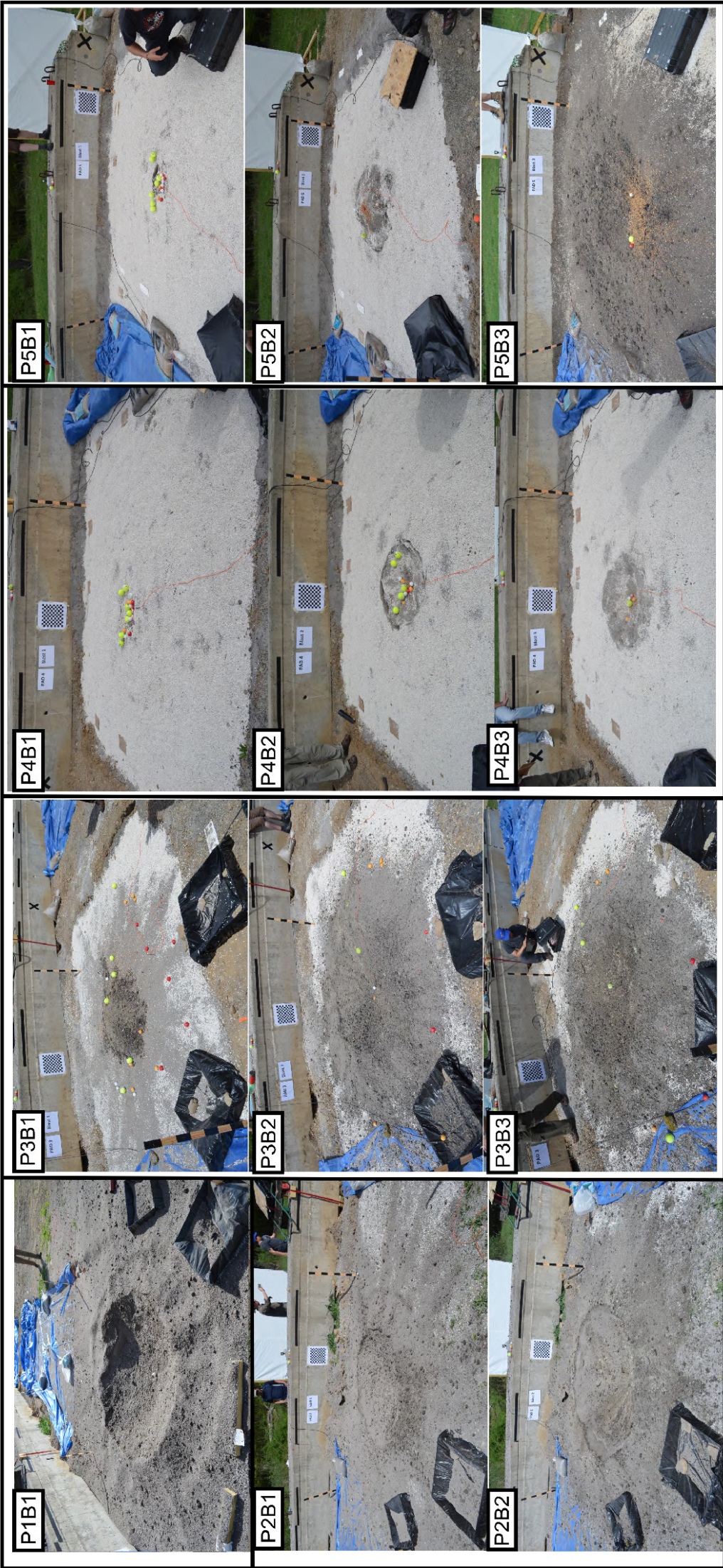
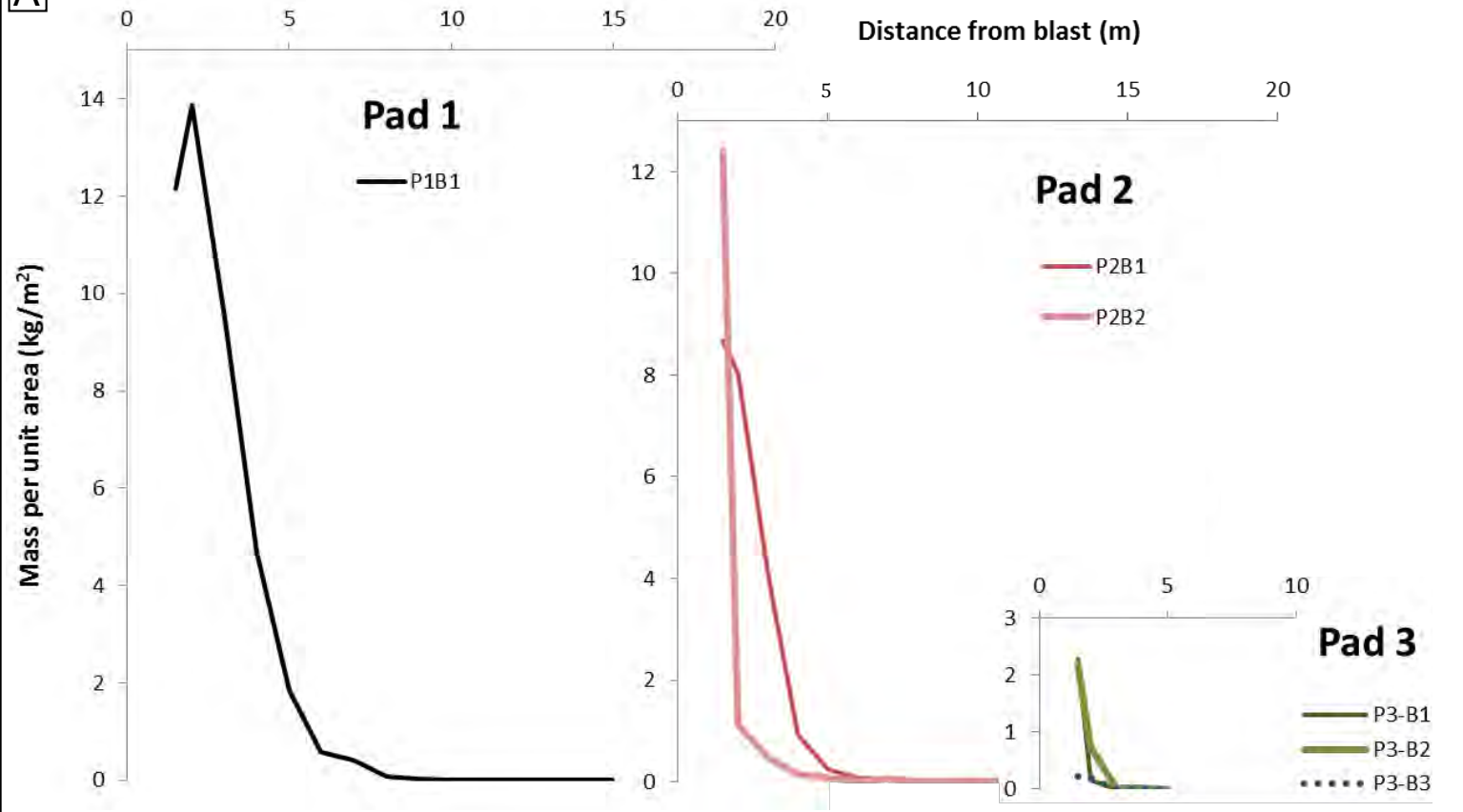
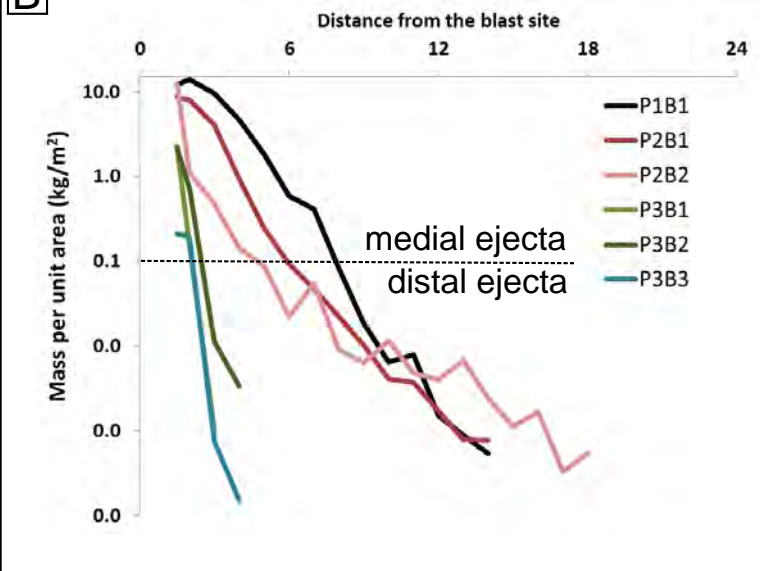
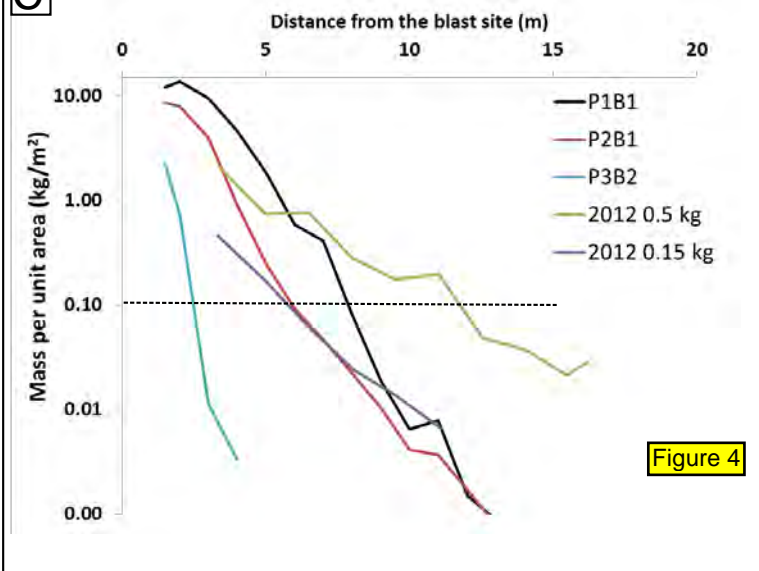


Figure 3

**A****B****C****Figure 4**

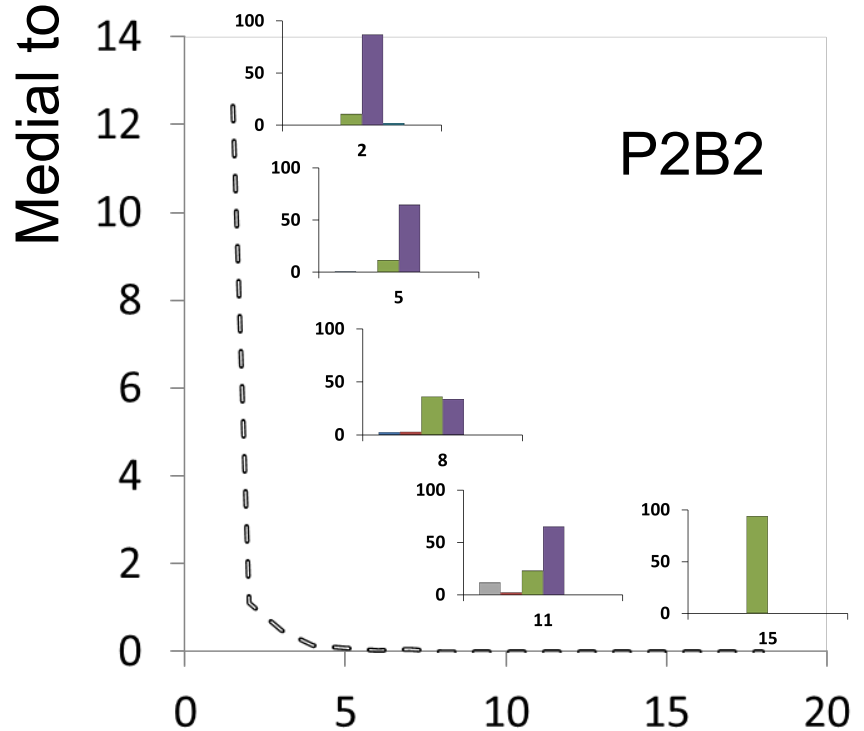
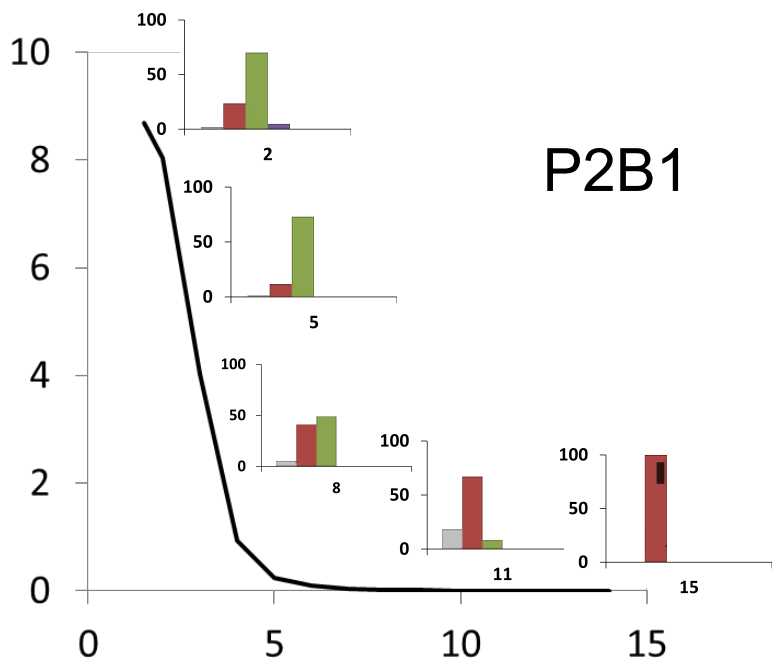
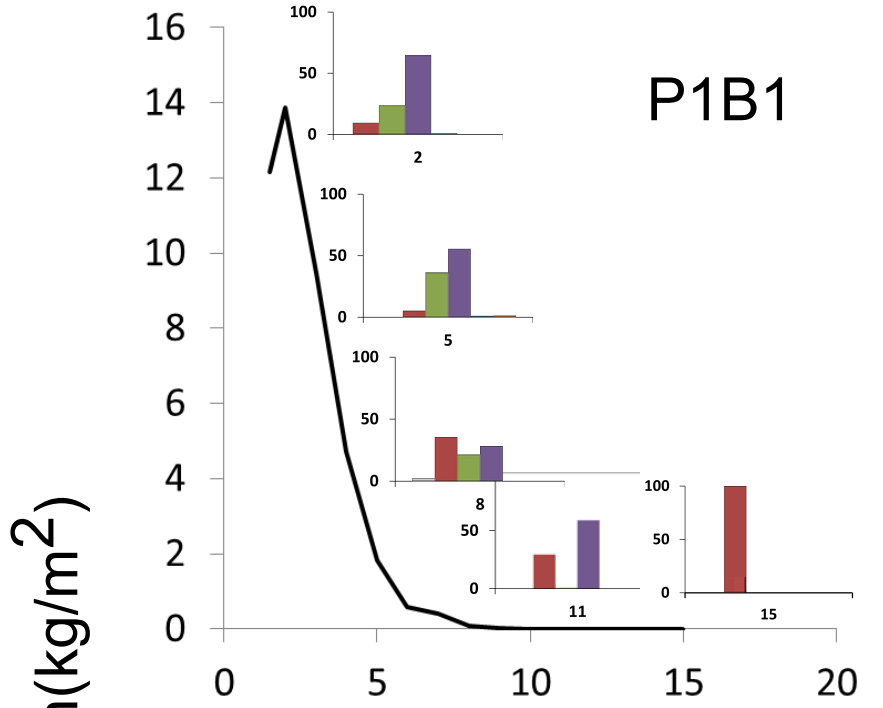
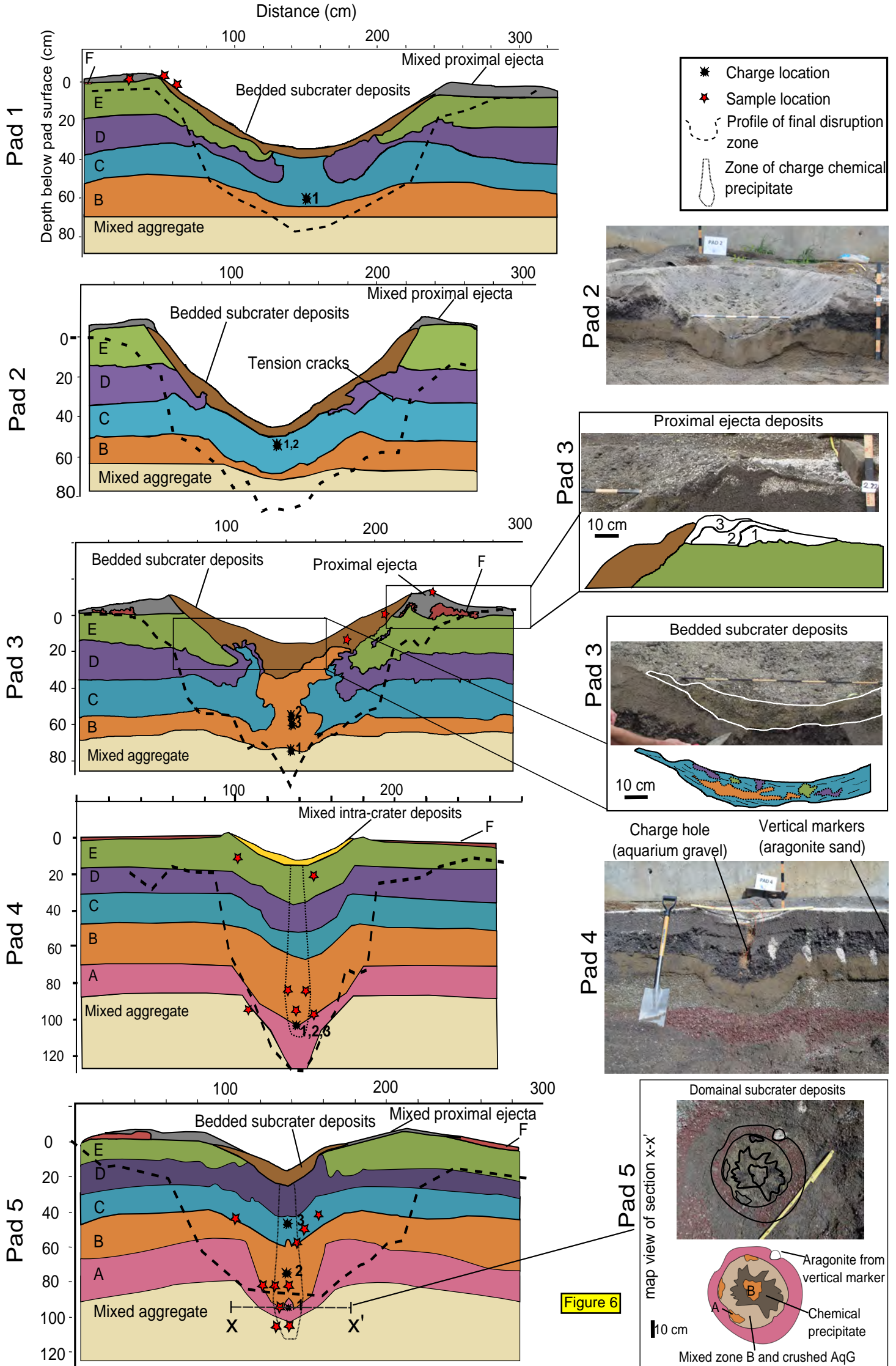


Figure 5

Distance from blast epicenter (m)



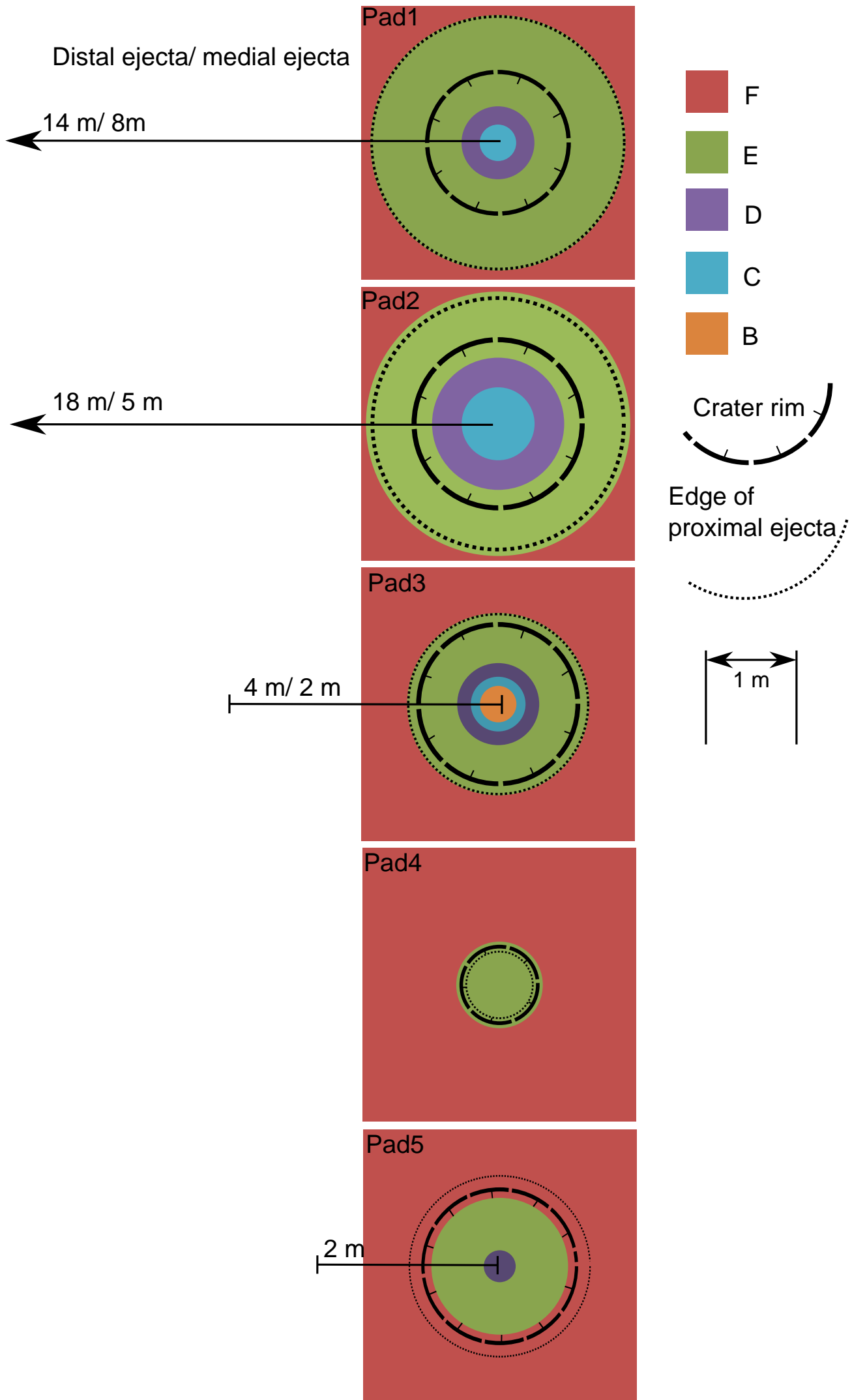


Figure 7

# Pad 3

Blast 1

Wt/Wb 0.77



Blast 2

Wt/Wb 1.37



Blast 3

Wt/Wb 0.96



# Pad 4

Blast 1

Wt/Wb 0.29



Blast 2

Wt/Wb 0.30



Blast 3

Wt/Wb 0.51



# Pad 5

Blast 1

Wt/Wb 0.20



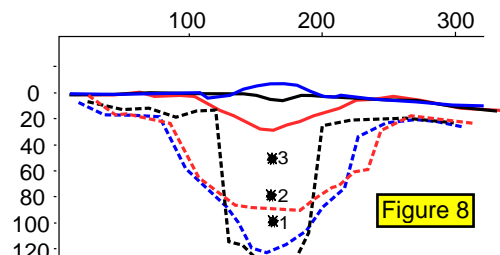
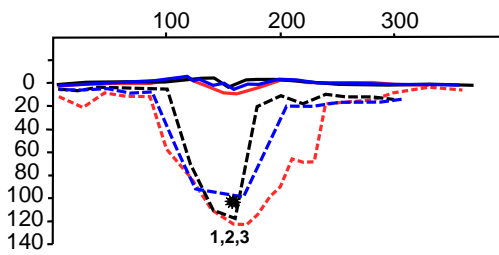
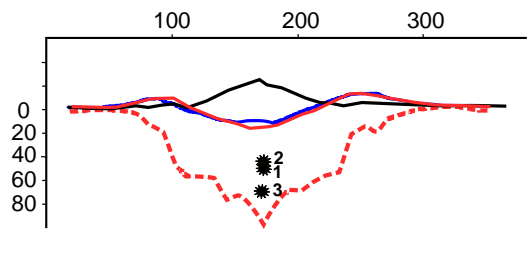
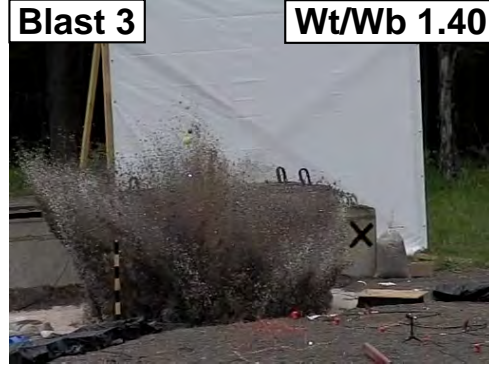
Blast 2

Wt/Wb 0.15



Blast 3

Wt/Wb 1.40



# Pad 2

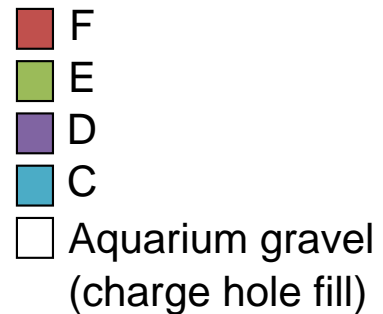
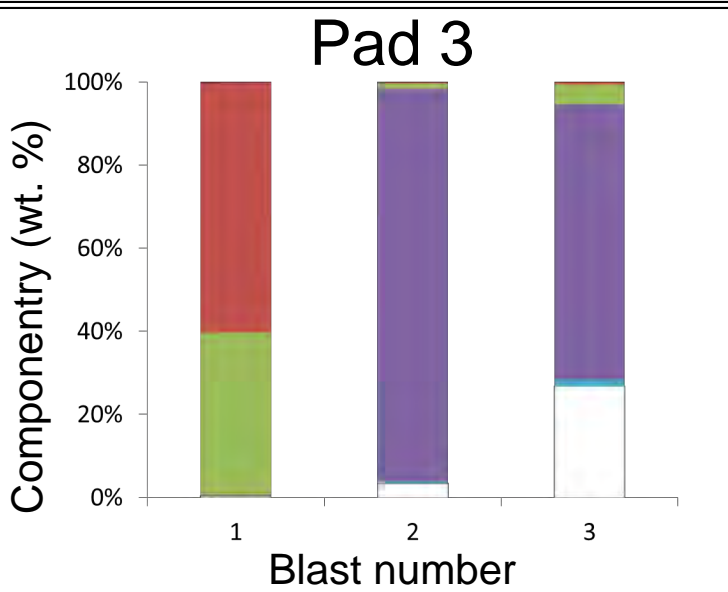
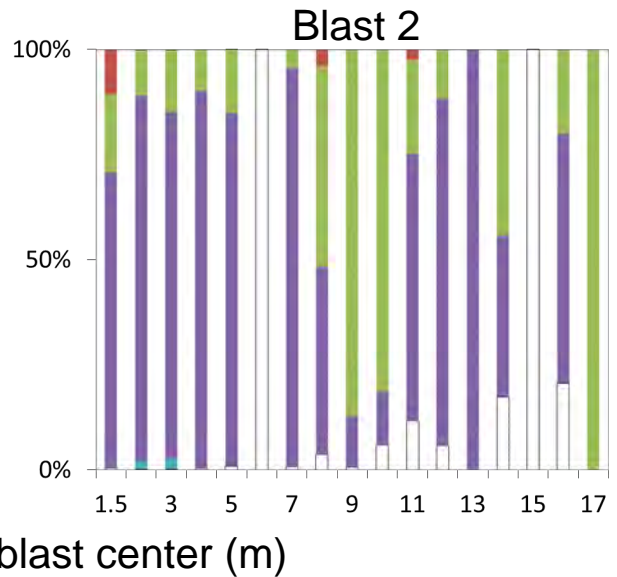
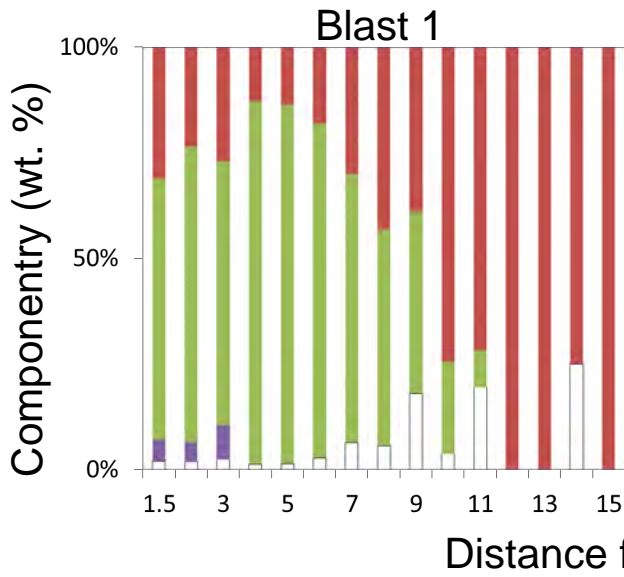
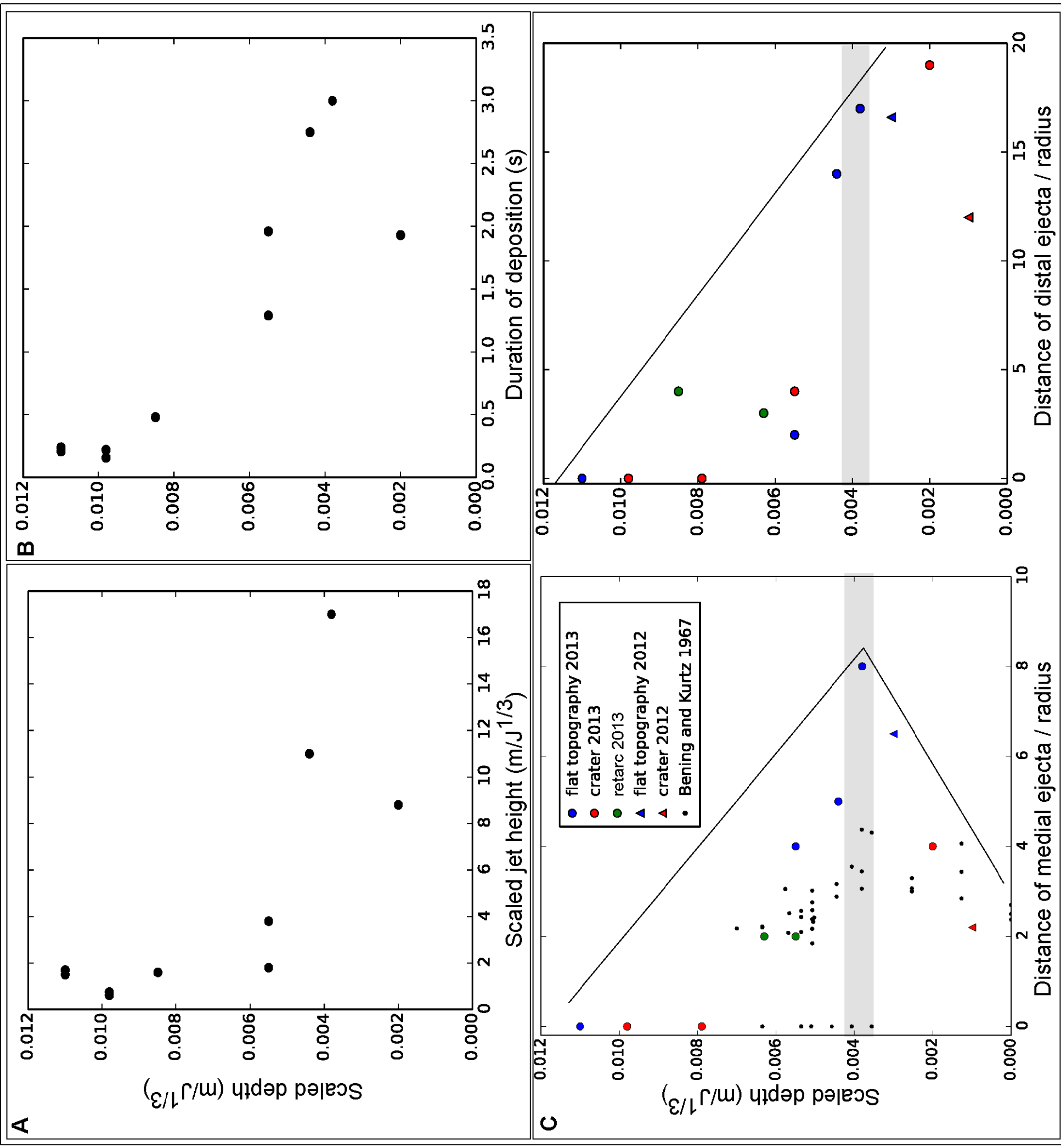


Figure 10



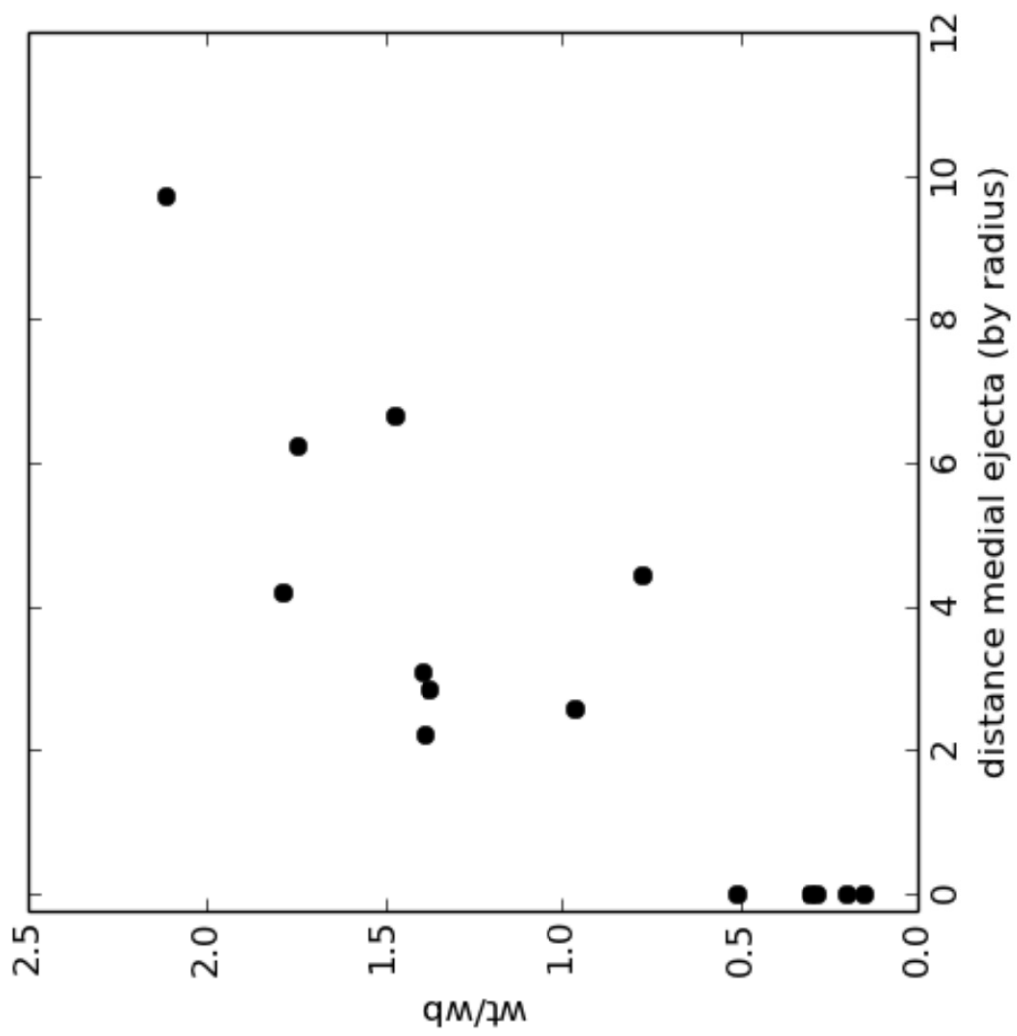
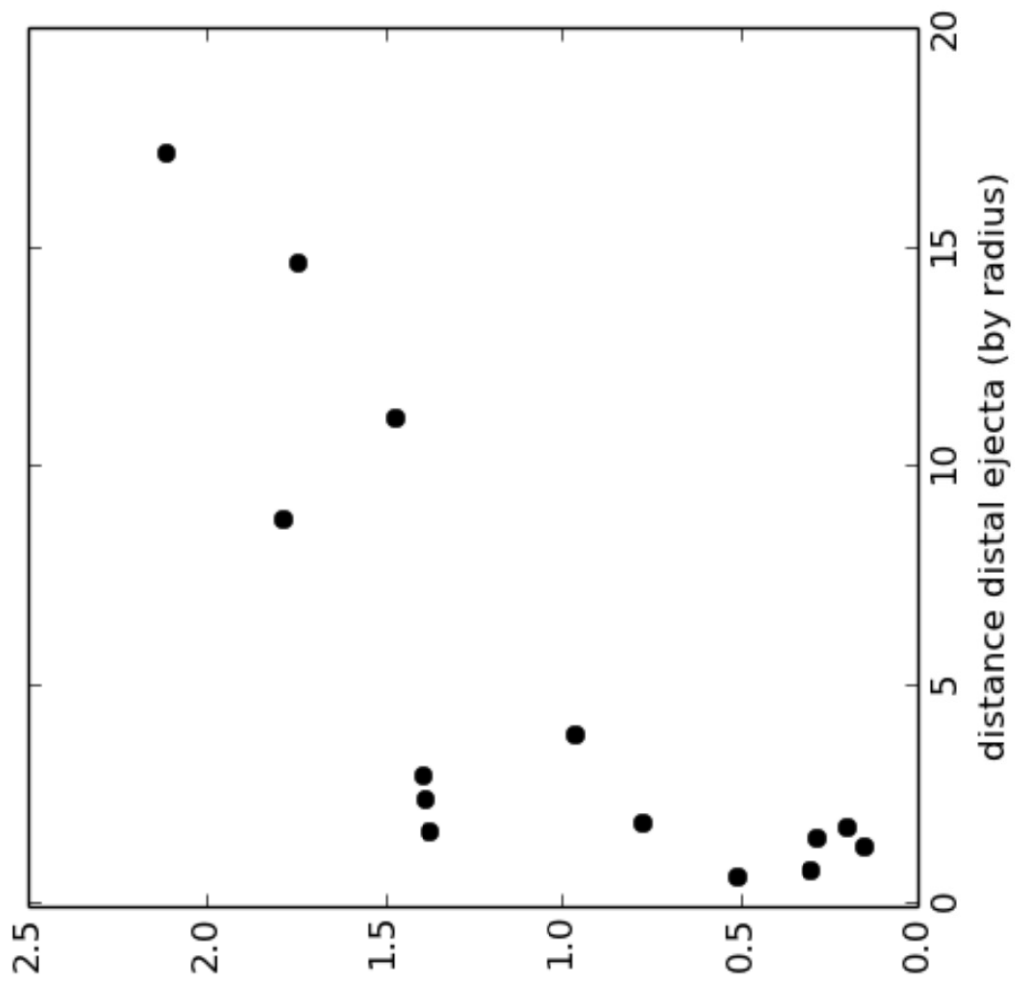


Figure 11

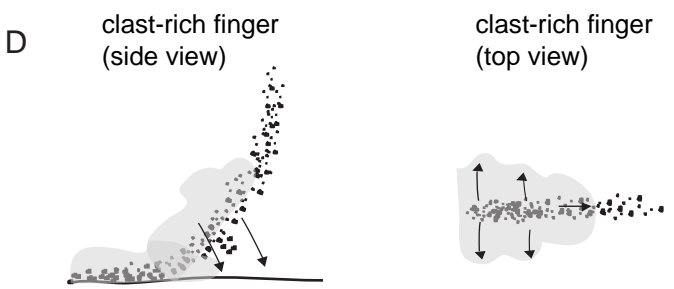
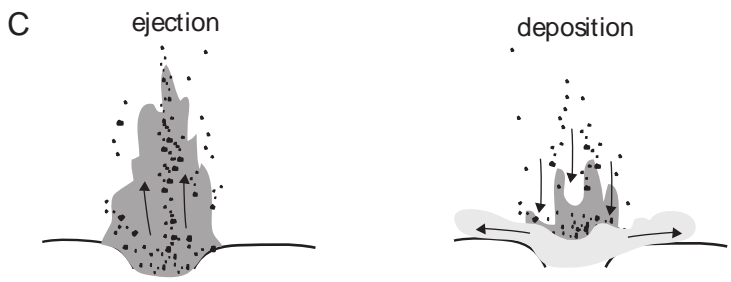
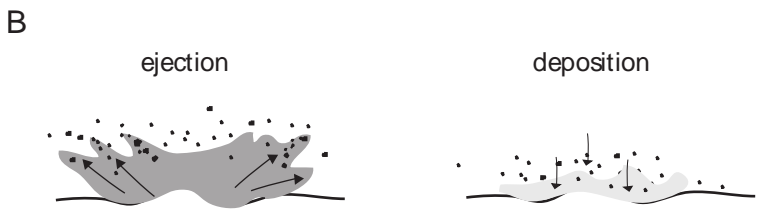
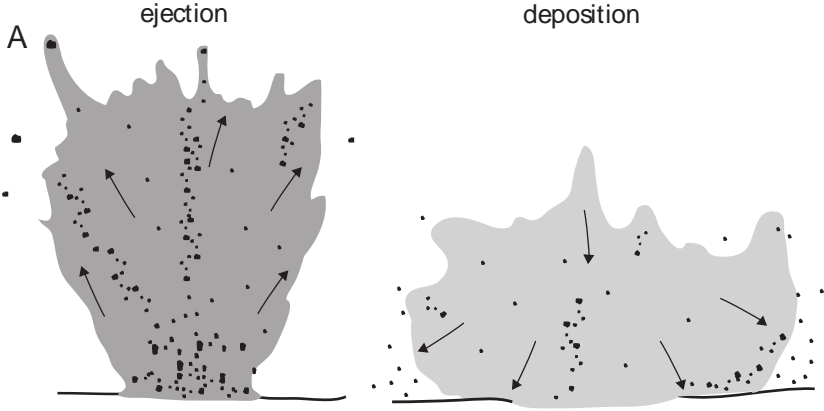


Figure 12

# Suoana Crater, Miyakejima Japan



Pad 3 excavation this study

2013 Experiments

Geshi et al. 2011

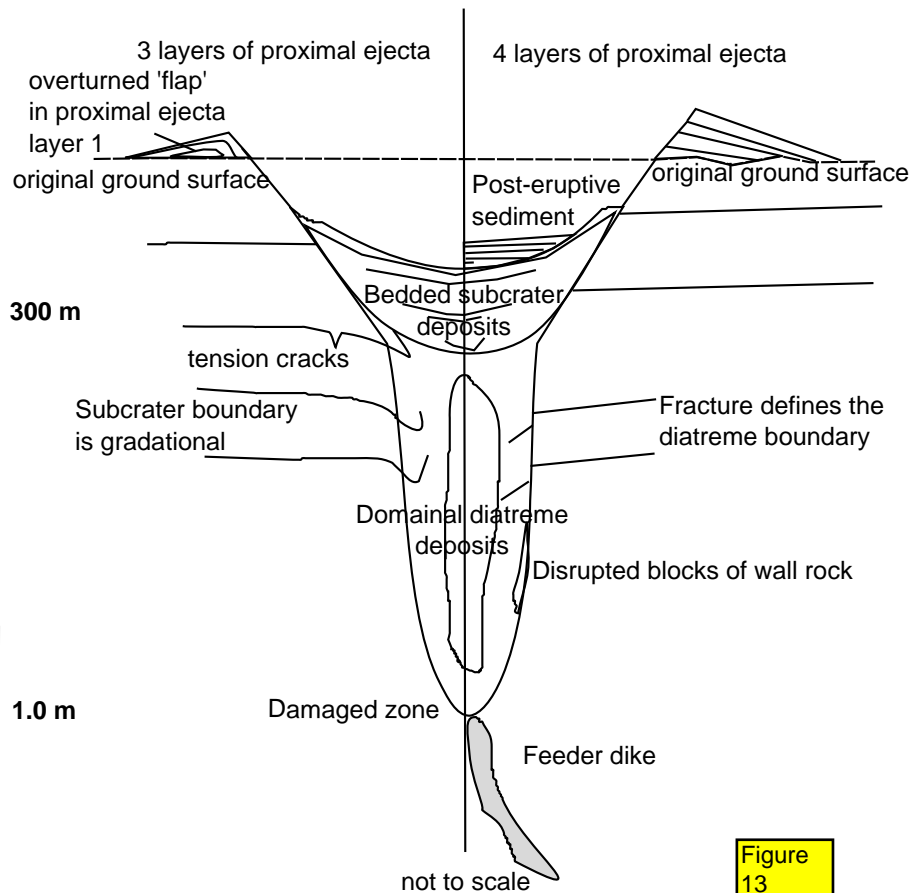


Figure 13